

# Open Research Online

---

The Open University's repository of research publications and other research outputs

## On the characteristics of internal tides and coastal upwelling behaviour in Marguerite Bay, west Antarctic Peninsula

### Journal Item

How to cite:

Wallace, Margaret I.; Meredith, Michael P.; Brandon, Mark A.; Sherwin, Toby J.; Dale, Andrew and Clarke, Andrew (2008). On the characteristics of internal tides and coastal upwelling behaviour in Marguerite Bay, west Antarctic Peninsula. *Deep-Sea Research Part II: Topical Studies in Oceanography*, 55(18-19) pp. 2023–2040.

For guidance on citations see [FAQs](#).

© 2008 Elsevier Ltd.

Version: Accepted Manuscript

Link(s) to article on publisher's website:

<http://dx.doi.org/doi:10.1016/j.dsr2.2008.04.033>

---

Copyright and Moral Rights for the articles on this site are retained by the individual authors and/or other copyright owners. For more information on Open Research Online's data [policy](#) on reuse of materials please consult the policies page.

---

[oro.open.ac.uk](http://oro.open.ac.uk)

2  
3  
4 **On the characteristics of internal tides and coastal upwelling**  
5 **behaviour in Marguerite Bay, west Antarctic Peninsula**

6  
7  
8 Margaret I. Wallace<sup>1,2\*</sup>, Michael P. Meredith<sup>2</sup>, Mark A. Brandon<sup>1</sup>, Toby J. Sherwin<sup>3</sup>,  
9 Andrew Dale<sup>3</sup>, Andrew Clarke<sup>2</sup>

10  
11 <sup>1</sup> Centre for Earth, Planetary, Space and Astronomical Research, The Open  
12 University, Walton Hall, Milton Keynes, U.K, MK6 7AA.

13 <sup>2</sup> British Antarctic Survey, High Cross, Madingley Road, Cambridge, U.K, CB3 0ET.

14 <sup>3</sup> The Scottish Association for Marine Science, Dunstaffnage Marine Laboratory,  
15 Oban, Argyll, U.K, PA37 1QA.

16  
17  
18 Margaret Wallace (corresponding author): [m.i.wallace@open.ac.uk](mailto:m.i.wallace@open.ac.uk)

19 Tel: +44 (0)1223 221260

20 Fax: +44 (0)1223 221226

21 Michael Meredith: [mmm@bas.ac.uk](mailto:mmm@bas.ac.uk)

22 Mark Brandon: [m.a.brandon@open.ac.uk](mailto:m.a.brandon@open.ac.uk)

23 Toby Sherwin: [Toby.Sherwin@sams.ac.uk](mailto:Toby.Sherwin@sams.ac.uk)

24 Andrew Dale: [Andrew.Dale@sams.ac.uk](mailto:Andrew.Dale@sams.ac.uk)

25 Andrew Clarke: [accl@bas.ac.uk](mailto:accl@bas.ac.uk)

26

## Abstract

27

28 Internal waves and coastal upwelling have important roles in both physical  
29 oceanography and marine ecosystems, via processes such as mixing of water masses  
30 and transfer of heat and nutrients to biologically active layers. In this paper we use  
31 quasi-weekly hydrographic profiles and moored records of temperature, salinity and  
32 water velocity to investigate the nature of internal tides and coastal upwelling  
33 behaviour in northern Marguerite Bay at the western Antarctic Peninsula. Within  
34 Ryder Bay, a near-coastal site in northern Marguerite Bay, atmospherically-forced  
35 oscillations of the water column with periods around 2-7 days are observed,  
36 associated with wind-induced coastal upwelling and downwelling. Sea ice cover is  
37 seen to play a role in the seasonal suppression of these oscillations. Significant  
38 internal tides are also observed at this site. A range of processes are seen to be  
39 important in controlling internal tide variability, including changes in local  
40 stratification and sea ice conditions. Both diurnal and semi-diurnal internal tidal  
41 species are observed, despite the study region being poleward of the critical latitude  
42 for diurnal internal tides. This suggests that at least the diurnal internal tides are  
43 generated close to the study location, and we investigate likely sources. Our work  
44 adds understanding to how such phenomena are generated, and what controls their  
45 variability, in a region of rapid physical change and profound ecosystem importance.

46

47

48

49 **Keywords:** Coastal upwelling, Internal tides, Sea ice, Antarctic Peninsula, Marguerite

50 Bay

51 **1. Introduction**

52

53 Both ocean upwelling and internal gravity waves are key phenomena in physical  
54 oceanography and have an impact upon marine ecology. Coastal upwelling and  
55 downwelling arise predominantly as a result of alongshore wind stress and the  
56 divergence of Ekman transport at the coast (Mitchum & Clarke, 1986), such that the  
57 tilt in the upwelled density structure is balanced by alongshore geostrophic flow.  
58 Coastal upwelling is predominantly an advective process that can lead to increased  
59 biological productivity, as the deep, upwelled waters are often nutrient-rich compared  
60 with those at the surface (e.g. Halpern, 1976; Winant, 1980; Small & Menzies, 1981).  
61 Conversely, downwelling has the potential to move biomass out of the light-  
62 favourable, shallow water environment, whilst both mechanisms can disrupt stable  
63 stratification via processes such as convection and mixing, leading to low gradients in  
64 properties such as density, temperature, salinity and chlorophyll.

65

66 Internal waves can also lead to mixing, particularly where interaction of the wave  
67 with topography leads to reflection and breaking, and potential redistribution of heat,  
68 salt and nutrients. There has been significant work on the barotropic-to-baroclinic  
69 tidal energy transfer at fjord sills (see Stigebrandt, 1999, for a review), and numerous  
70 studies have concluded that the vertical mixing and circulation in fjords is  
71 predominantly driven by such processes (e.g. Stigebrandt, 1976; Stigebrandt & Aure,  
72 1989; Simpson & Rippeth, 1993). The interaction between internal waves and the  
73 seabed may induce wave breaking, the formation of local regions of high shear, and  
74 enhanced turbulence; these lead to dissipation of the internal wave energy (e.g. Polzin  
75 et al., 1997). Similar processes have been observed on the continental shelf (New,

76 1988; Sherwin, 1988; New & Pingree, 1990; Rippeth & Inall, 2002), whilst diapycnal  
77 mixing in the deep ocean away from topography is also driven predominantly by  
78 internal wave activity (Munk & Wunsch, 1998). Internal tides have been observed in  
79 both the Arctic (Konyaev et al., 2000; Konyaev, 2000; Morozov et al., 2003) and the  
80 ocean close to Antarctica (Foldvik et al., 1990; Levine et al., 1997; Albrecht et al.,  
81 2006), and modelling work has suggested that these features are locally generated via  
82 the interaction of barotropic tides with seabed topography (e.g. Morozov & Pisarev,  
83 2002; Padman et al., 2006). However, the role of internal tides in mixing is not well  
84 constrained, and studies have shown that tidally-induced mixing can be small, even in  
85 the presence of energetic baroclinic tides (e.g. Muench et al., 2002; Padman et al.,  
86 2006).

87

88 Internal waves can arise from a number of sources, including the interaction of  
89 currents, such as barotropic tides and wind-induced flows, with seabed topography  
90 (e.g. New, 1988; Stigebrandt, 1999; Levine et al., 1997). Once generated, linear wave  
91 theory predicts that freely propagating waves are restricted to a frequency,  $\omega$ , where  
92  $f^2 < \omega^2$ , and  $f$  is the inertial frequency (LeBlond & Mysak, 1978). Thus, for any wave  
93 with a period greater than 12 hours, there is a critical latitude beyond which it cannot  
94 propagate freely because its frequency is less than  $f$ . In reality, seabed topography  
95 disrupts this simple theory (LeBlond & Mysak, 1978), and internal waves can be  
96 generated poleward of the critical latitude and propagate along a bathymetric barrier  
97 (such as the coastline or a sloping bottom), confined to within approximately one  
98 internal Rossby radius of the barrier (Emery & Thomson, 2004). The critical latitude  
99 for a diurnal internal tide is  $\sim 30^\circ$  in both hemispheres, whilst those for the M2 and S2  
100 semidiurnal internal tides are  $\sim 75^\circ$  and  $\sim 85^\circ$ , respectively, placing all polar oceans

101 beyond the critical latitude for diurnal internal tides and some beyond those for  
102 semidiurnal internal tides. Here, we investigate observations of both internal tides and  
103 atmospherically forced coastal upwelling/downwelling in Marguerite Bay, west  
104 Antarctic Peninsula, between January 2005 and April 2007.

105

## 106 **2. Western Antarctic Peninsula shelf waters**

107

108 The western Antarctic Peninsula (WAP) shelf (Figure 1) [**insert Figure 1 here**] is  
109 deep compared with most of the world's shelf seas (much of the shelf is >500m deep),  
110 and features rough bathymetry and numerous deep troughs ( $\leq 1600\text{m}$ ) carved by  
111 glacial scouring. Offshore of the WAP shelf slope lies the southern boundary of the  
112 Antarctic Circumpolar Current (ACC; e.g. Hofmann & Klinck, 1998; Klinck, 1998),  
113 which brings warm, saline Circumpolar Deep Water (CDW) close to the slope, from  
114 where it can access the shelf (e.g. Martinson et al., this issue). The glacial troughs are  
115 preferential routes for this intrusion of CDW, and the less-dense variety of this water  
116 mass (Upper CDW; UCDW) in particular accesses the shelf via this route (Klinck et  
117 al., 2004). Above UCDW lies the seasonally-varying Antarctic Surface Water  
118 (AASW), which is separated from the underlying waters by a permanent pycnocline  
119 at ~150-200m (Beardsley et al., 2004; Hofmann & Klinck, 1998; Smith et al., 1999).  
120 The depth of this boundary is linked to sea ice conditions, with a generally deeper  
121 pycnocline in years with sea ice production greater than the temporal mean (Smith &  
122 Klinck, 2002; Meredith et al., 2004). Vertical transfer of heat across the pycnocline  
123 from the UCDW to AASW leads to relatively low rates of sea ice production in the  
124 area, ensuring that surface waters under present climate conditions do not become  
125 denser than the underlying modified UCDW and thereby prohibiting the formation of

126 dense deep and bottom waters (Martinson et al., this issue). During winter, pack ice  
127 covers the shelf and the surface layer is uniformly mixed to 100m depth or more, with  
128 water at or near the freezing point (temperature,  $T$ ,  $\sim -1.8^{\circ}\text{C}$ ) (Smith et al., 1999;  
129 Meredith et al., 2004). Salinity is increased via brine rejection during ice production,  
130 resulting in mixed-layer salinity,  $S$ , of approximately 34.1 during winter (Toole, 1981;  
131 Klinck et al., 2004). In summer, shallow surface layers (20-30m) are freshened by ice  
132 melt and warmed by solar heating; these overlie the remnant of the winter mixed  
133 layer, which is now termed Winter Water (WW). This persists during summer as a  
134 relative vertical minimum in temperature at  $\sim 70$ -100m (Klinck, 1998; Klinck et al.,  
135 2004), though occasionally as deep as 150m (Meredith et al., 2004). Over summer and  
136 autumn, increased storm activity leads to the breakdown of these layers and remnant  
137 WW undergoes mixing with surface and subpycnocline waters, leading to erosion of  
138 the WW signature in areas such as Ryder Bay (Meredith et al., 2004). This does not  
139 appear to be a shelf-wide process, however, as data from west of Adelaide Island  
140 show the presence of the typical WW minimum well into autumn (e.g. Klinck et al.,  
141 2004).

142

143 On the WAP shelf, UCDW intrusions mix with AASW to produce modified UCDW,  
144 which has properties intermediate between the two water masses, and are thus crucial  
145 for the heat and salt budgets of the region (Hofmann & Klinck, 1998; Klinck, 1998;  
146 Smith et al., 1999; Smith & Klinck, 2002; Martinson et al., this issue). Several studies  
147 suggest that internal wave activity and localised mixing over the rugged topography  
148 may play a role in this process (Klinck, 1998; Smith & Klinck, 2002; Dinniman &  
149 Klinck, 2004), whilst Howard et al. (2004) concluded that coastal upwelling could be  
150 a significant factor contributing to the upward flux of UCDW properties and has the

151 potential to raise UCDW into the depth range affected directly by surface stress. The  
152 role of these processes in mixing is the subject of ongoing investigations.

153

154 Due to its high primary productivity, the WAP continental shelf supports a large  
155 biomass of Antarctic krill (Ross et al., 1996a), and consequently large populations of  
156 higher predators such as penguins (Fraser & Trivelpiece, 1996) and seals (Costa &  
157 Crocker, 1996). This biological productivity is strongly linked to physical processes  
158 (Ross et al., 1996b), so internal wave- or upwelling-induced disruption of  
159 stratification, both of which influence nutrient and phytoplankton distribution (e.g.  
160 Small & Menzies, 1981; Ostrovsky et al., 1996; Mackinnon & Gregg, 2005), have the  
161 potential to affect the entire marine ecosystem of the region. Such mixing is also  
162 known to influence the redistribution of heat in the upper ocean (e.g. Gregg, 1987;  
163 Mackinnon & Gregg, 2005; Winant, 1980), which has the potential to influence sea  
164 ice conditions, whilst tidally-forced currents are known to influence sea ice conditions  
165 via processes such as lead formation (e.g. Kowalik & Proshutinsky, 1994; Wadhams,  
166 2000; Koentopp et al., 2005). Therefore, both coastal upwelling/downwelling and  
167 internal wave activity can be expected to have a significant impact upon a seasonally  
168 sea ice-covered region of high biological productivity such as Marguerite Bay. In this  
169 paper we investigate these phenomena, using a combination of observational data and  
170 theoretical considerations.

171

### 172 **3. Methods**

173

174 To investigate internal wave and coastal upwelling activity in northern Marguerite  
175 Bay we use two data sources. The first is part of the British Antarctic Survey's



176 Rothera Biological and Oceanographic Time Series Study (RaTS; Clarke et al., this  
177 issue). As part of RaTS, a year-round time series of conductivity-temperature-depth  
178 (CTD) profiles from a nearshore location in Ryder Bay (a small embayment at the  
179 northern end of Marguerite Bay; 67°34.20'S, 68°13.50'W; 520m water depth; Figure  
180 1) has been collected since 1998. These data have been supplemented in recent years  
181 by our second source of data: fixed moorings at both the RaTS site (location above)  
182 and an offshore location in a deep glacial trough on the WAP continental shelf (67°  
183 55.39'S, 68° 24.15'W; 840m water depth; Figure 1). This trough lies off the main axis  
184 of Marguerite Trough and the mooring is hereafter referred to as MT. In this paper,  
185 we focus on data from the quasi-weekly RaTS CTD casts in conjunction with moored  
186 CTD, temperature-depth recorder (TDR), temperature recorder (TR) and Acoustic  
187 Doppler Current Profiler (ADCP) time series from both moorings.

188

189 Moored data are summarized in Table 1 [**insert Table 1 here**] and were collected  
190 from the RaTS site for January 2005 – April 2007 (three consecutive deployments)  
191 over the depth range ~0-280m, and from MT for January 2005 – January 2006 (one  
192 deployment) over the depth range ~0-564m. In this paper, we refer to each RaTS  
193 mooring deployment by its number within the sequence (1, 2 or 3), the timings of  
194 which are detailed in Table 1. A delay in the intended recovery and redeployment of  
195 the moorings in January 2006 led to a data gap of roughly three weeks in all sensors  
196 except the ADCPs, which had sufficient onboard data storage to allow uninterrupted  
197 collection up to recovery in mid-February. The MT mooring was lost during the  
198 second deployment, hence the collection of only one year of data at this site.

199

200 The moored CTDs, TDRs and TRs were manufactured by Richard Branckner  
201 Research (RBR) Ltd, and were configured to collect data at hourly intervals, whilst  
202 the 75kHz Workhorse Long Ranger ADCPs (RD Instruments) averaged data into 15-  
203 minute ensembles. At the RaTS site the RBR sensors were separated vertically by  
204 between 15 and 35m within the depth range expected to sample modified UCDW  
205 (below 200m). The upward-looking ADCP, at ~200m, measured the velocity profile  
206 of the upper water column with a vertical resolution of 4m and a velocity resolution of  
207  $1\text{mms}^{-1}$ . At MT, the upward looking ADCP (bin depth and velocity resolution as  
208 above), was located at ~115m, and the RBR sensors below ~185m at intervals of ~50-  
209 70m. Deployment depths and sample recording rates for each instrument are detailed  
210 in Table 2 **[insert Table 2 here]**.

211

212 The CTD profiles at the RaTS site were carried out roughly 1-2 times per week from  
213 January 2005 – April 2007, using a SeaBird Electronics SBE-19 instrument.

214 Deployment was from a small boat during the summer and through the sea ice cover  
215 from a sledge during winter, given favourable ice conditions. Further details on data  
216 collection can be found in Meredith et al. (2004), Clarke et al (this issue) and Wallace  
217 (2007).

218

219 Surface meteorological data were obtained from Rothera Research Station, courtesy  
220 of the British Antarctic Survey. Hourly values of wind direction and speed were  
221 collected for three 30-day periods for the summer and winter of the first two RaTS  
222 mooring deployments and the summer of the third RaTS deployment. Linear  
223 interpolation was used to fill gaps in the wind time series, where not more than five  
224 consecutive data points were missing.

225 This analysis also makes use of the AntPen04.01 tide model (Padman, unpublished;  
226 [www.esr.org/ptm\\_index](http://www.esr.org/ptm_index)), which is a high-resolution ( $1/30^\circ$  longitude by  $1/60^\circ$   
227 latitude,  $\sim 2\text{km}$ ) forward model, based on the shallow water equations, and forced at  
228 the open boundary by tide heights from the circum-Antarctic forward model  
229 (CATS02.01; Padman et al., 2002) and by astronomical forcing. The model is tuned  
230 to data using a linear benthic drag coefficient.

231

#### 232 **4. Results**

233

234 Internal waves are observed in our data from Marguerite Bay at both diurnal and  
235 semidiurnal tidal frequencies, in addition to quasi-periodic fluctuations on timescales  
236 of a few days. The latter longer-period fluctuations appear to be atmospherically-  
237 forced, and are investigated in Section 4.1, whilst the internal tides are explored in  
238 Section 4.2. Characteristic profiles of potential temperature,  $\theta$ ,  $S$ , potential density  
239 anomaly,  $\sigma_\theta$ , and buoyancy frequency,  $N$ , from the RaTS site, along with a  
240 comparison of  $\theta$  from the two mooring sites for the summers of 2005-2007 are shown  
241 in Figure 2 [**insert Figure 2 here**], and will be referred to throughout the following  
242 analyses.  $N$  is derived from the gravitational acceleration,  $g$ , the reference density at  
243 depth  $z$ ,  $\rho_0$ , and the vertical density gradient,  $d\rho/dz$  (Pond & Pickard, 1983):

244

$$245 \quad N(z) = \sqrt{\frac{-g}{\rho_0} \frac{d\rho}{dz}} \quad (1)$$

246

247

248

#### 249 *4.1 Atmospherically-forced fluctuations*

250

251 Figure 3 [insert Figure 3 here] shows  $T$ ,  $S$  and  $\sigma_\theta$  time series from the RaTS site,  
252 along with the horizontal velocity from the ADCP bin immediately below the surface,  
253 while Figure 4 [insert Figure 4 here] shows the corresponding  $T$  and ADCP data  
254 from the MT site. All time series are filtered using a 26-hour Butterworth lowpass  
255 filter to remove tidal and higher frequency variability. Markedly low variance in the  
256 ADCP data is indicative of the presence of sea ice above the mooring (e.g. Visbeck &  
257 Fischer, 1995; Hyatt et al., 2008) and shaded in grey on Figures 3 and 4. At the RaTS  
258 site in both 2005 and 2006 there were 3-4 weeks of ice cover, followed by 2-3 weeks  
259 of open water before the onset of pack ice. Ryder Bay may, in fact, be covered by fast  
260 ice for much of the winter, whilst the offshore regions of Marguerite Bay are covered  
261 in pack ice. Therefore, for simplicity, we will refer to all high concentration ice cover  
262 as ‘pack ice’. We term periods interpreted as being pack ice covered as the ‘ice-  
263 covered season’, and periods of open water and those of brief ice cover the ‘ice-free  
264 season’.

265

266 Quasi-periodic fluctuations on timescales of  $\sim$ 2-7 days have been observed in certain  
267 sections of the moored time series from the RaTS site (an example of the signal is  
268 marked by the grey oval on Figure 3), but are not observed at the MT mooring (Figure  
269 4). Their signal is variable both in magnitude and duration, and is observed in all of  
270 the RaTS temperature loggers (CTDs, TR, TDR), although the magnitude of the  
271 signal decreases with depth, which is consistent with the lower gradients observed  
272 deeper in the water column (Figure 2). The fluctuations can also be seen in  $S$  and  $\sigma_\theta$  at  
273 the uppermost CTD (199m), but are more difficult to identify in these time series at

274 the deeper sensors, due to lower signal-to-noise ratios compared with those in  $T$   
275 (Wallace, 2007). Thus, our analysis will concentrate upon  $T$  data. The thermohaline  
276 properties of UCDW are relatively invariant (Hofmann & Klinck, 1998; Wallace,  
277 2007), and at the RaTS site temperature below the WW minimum at the RaTS site  
278 consistently increases with depth (Meredith et al., 2004; Wallace, 2007). Thus, for  
279 this location, and for our specific purposes, isotherms can be considered analogous to  
280 isopycnals in UCDW and  $T$  can reasonably be considered a proxy for  $\sigma_\theta$ , allowing  
281 more complete coverage of the water column than density time series would allow.

282

283 The fluctuations are apparently unaffected by the initial periods of ice cover, but are  
284 smaller in magnitude in the presence of pack ice. A high degree of interannual  
285 variability is also observed, with the fluctuations being most pronounced in Feb-Jun  
286 during deployment 2 (2006). Although reduced during the ice-covered season, the  
287 signal is clearly visible during 2006, whereas during 2005 it is difficult to distinguish  
288 in the presence of ice. In 2007 the fluctuations only become apparent in March, after  
289 the region has been ice-free for more than two months.

290

291 The temporal and spatial variability of the temperature fluctuations is best illustrated  
292 by means of power spectral analysis, which partitions variance as a function of  
293 frequency (Emery & Thompson, 2004). Figure 5a [**insert Figure 5 here**] shows  
294 power spectral density (PSD) for all temperature sensors during the ice-free season of  
295 deployment 2, when the fluctuations are observed most clearly. Several peaks are  
296 consistently present at different depths over this frequency range, and the decrease in  
297 variance with depth can be clearly observed. Hence, comparison between the different  
298 deployments and between the two mooring sites (Figure 5b and 5c) requires the

299 selection of time series from similar depths. The instruments at 283m, 274m and  
300 273m for the three RaTS deployments, respectively, and 298m for MT are most  
301 appropriate for this. The spectra in Figures 5b and 5c show several features of note:  
302 (1) variability in the 2-7 day band is consistently higher at the RaTS site than at MT;  
303 (2) RaTS deployment 2 shows the strongest variability; and (3) the difference in  
304 depths between the sensors is unlikely to be the most important factor in the observed  
305 differences between the spectra, as the sensors from RaTS deployments 2 and 3 are at  
306 virtually the same depth, yet show markedly different variability (i.e. the influence of  
307 time is strong compared with that of depth). Figure 5d illustrates the difference  
308 between the RaTS and MT sites, where spectra for each site, along with their 95%  
309 confidence intervals, show that the RaTS site experiences stronger variability in the 2-  
310 7 day band than is observed at MT. This is unlikely to arise from differences in  
311 temperature gradients between the two sites, as they are virtually identical below  
312 ~200m during the summers of 2005, 2006 and 2007 (Figure 2c). Finally, Figure 5e  
313 illustrates the difference between the ice-free and ice-covered seasons for RaTS  
314 deployment 2, such that variability in the 2-7 day band is clearly higher in the absence  
315 of ice.

316

317 The ~2-7 day fluctuations are most readily interpreted as oscillations of isotherms,  
318 and the broad frequency range of the oscillations indicates that they are forced by a  
319 strongly variable mechanism operating on a timescale of several days. The most  
320 obvious explanation for the observations is thus an oceanic response to wind forcing.  
321 Supporting this concept, temperature anomaly time series over the ice-free season  
322 correlate significantly with wind anomalies measured at Rothera, which are known to  
323 differ from those elsewhere on the WAP because of local topography (Beardsley et

324 al., 2004). The oscillation is sensitive to wind direction, with the strongest correlation  
325 associated with northwest to southeastward winds. Correlations are positive with  
326 northwestward winds and negative with southeastward winds, indicating that the  
327 former lead to warming and the latter to cooling. Examples of the correlations are  
328 shown in Figure 6 [insert Figure 6 here] for the shallowest (CTD10822 at 202m) and  
329 deepest (CTD10824 at 286m) temperature sensors at the RaTS site for the 30-day  
330 period 26<sup>th</sup> January – 24<sup>th</sup> February 2005. The intervening three temperature sensors  
331 show similar correlations. Winds lead the temperature signal by 27-36 hours, and the  
332 correlations decrease with depth in the water column, from 0.56 at 202m to 0.36 at  
333 286m. All correlations are significant at either the 95% or 99% level (statistical  
334 significance is calculated following the method of Trenberth, 1984). No significant  
335 correlations are observed during the ice-covered season, which is consistent with the  
336 observed decrease in the magnitude of the oscillation, indicating a seasonal cycle in  
337 the winds and/or the ocean's response to the atmospheric forcing. Spectral analysis of  
338 NW-SE winds from the ice-free season shows significant peaks over the 2-7 day  
339 period that correspond with those observed in temperature time series, as shown in  
340 Figure 7 [insert Figure 7 here] for deployment 2.

341

342 The significant lagged correlations with the winds are consistent with wind-driven  
343 upwelling and downwelling behaviour, whereby a northwestward wind (i.e. parallel to  
344 the coast; Figure 1b) tends to induce upwelling along the NE coast of Ryder Bay,  
345 leading to the observed temperature increase at depth, whilst a southeastward wind is  
346 associated with downwelling and a temperature decrease at depth. However, this  
347 simple correlation does not consider the cumulative response of the ocean to  
348 upwelling/downwelling favourable winds. For instance, Austin & Barth (2002) found

349 that an index of coastal upwelling/downwelling in the ocean off the coast of Oregon  
350 was a function of the weighted cumulative alongshore wind stress on a timescale of 2-  
351 8 days. Following their method, we examine the coastal upwelling response (i.e. the  
352 observed temperature fluctuations) to the cumulative NW-SE wind stress ( $W$ , positive  
353 NW-ward), weighted to the most recent observations, over the cumulative upwelling  
354 timescale ( $t_c$ ), according to the equation:

355

$$356 \quad W = \int_{t'=0}^t \tau^s e^{(t'-t)/t_c} dt' \quad (2)$$

357

358 where  $\tau^s$  is the NW-SE wind stress and  $t'$  is time. The analysis is carried out over three  
359 30-day periods for the ice-free and ice-covered season of each deployment (Table 3)  
360 **[insert Table 3 here]**. As previously, wind and oceanographic time series are filtered  
361 using a 26-hour Butterworth lowpass filter prior to analysis. Correlation of  
362 temperature time series with  $W$  for a number of different values of  $t_c$  reveal that  
363 upwelling/downwelling behaviour at the RaTS site responds to the cumulative NW-  
364 SE wind stress over a timescale of 17-90 hours. These results are in conceptual  
365 agreement with those of Austin & Barth (2002). Fewer significant correlations are  
366 observed during the ice-covered season, and possible explanations for this include: (1)  
367 seasonal changes in stratification, leading to a change in the ocean's response to wind  
368 forcing; (2) a seasonal cycle in the wind forcing; and (3) damping of the ocean's  
369 response to the atmosphere by the presence of sea ice. Each of these possibilities is  
370 discussed in turn.

371



372 (1) Figure 2 shows that buoyancy frequency is relatively stable below ~200m  
373 throughout the year, with only a small reduction in  $N$  during winter. This  
374 pattern is observed every year, and  $N$  is similar at these depths throughout the  
375 three deployments, yet the fluctuation clearly varies on both seasonal and  
376 interannual timescales. Figure 8 [insert Figure 8 here] shows time series of  
377 monthly mean NW-SE wind stress anomaly, buoyancy frequency anomaly at  
378 each of the sensor depths (derived from the RaTS CTD profile dataset) and  $t_c$   
379 for significant correlations between each temperature sensor and the  
380 cumulative NW-SE wind stress. Significant correlations with cumulative wind  
381 stress are observed at all depths in the presence of both high and low  $N$ , so  
382 although we can expect the observed temporal variability of the fluctuations to  
383 be influenced by changes in stratification, the observations cannot be solely  
384 attributed to this cause.

385 (2) The time series of wind stress anomaly in Figure 8 shows that winds are  
386 generally stronger during the ice-covered season, which does not explain the  
387 observed temporal variability in the temperature fluctuations. Furthermore,  
388 significant correlations occur between temperature and NW-SE wind stress  
389 both when winds are anomalously strong and when they are anomalously  
390 weak, so the observations cannot be explained in terms of wind stress  
391 variability alone.

392 (3) Periods of sea ice cover are marked on Figure 8. In the presence of ice, the  
393 number of significant correlations is reduced, implying that the sea ice has a  
394 significant effect upon the transmission of wind stress to the deep ocean. This  
395 concept is supported by the rapidity of the response of the fluctuations to the  
396 presence of sea ice. Observations from Rothera Station suggest that sea ice

397 cover was more fragmented in Ryder Bay in 2006 than 2005, which is  
398 consistent with the relative strengths of the fluctuations during the two  
399 winters. Whether the decrease in the fluctuations during the ice-covered  
400 season is a response to local sea ice conditions in Ryder Bay or those  
401 throughout the wider Marguerite Bay area cannot be determined without  
402 comprehensive, high resolution sea ice data across the region. Ryder Bay can  
403 be covered with fast ice whilst the ice in the rest of northern Marguerite Bay is  
404 fragmented, or *vice versa*, but several years' worth of data from both locations  
405 would be needed, along with comprehensive sea ice observations, to unravel  
406 such connections.

407

408 The internal Rossby radius of deformation ( $r$ ) sets the offshore length scale over  
409 which the influence of coastal upwelling is discernible. This can be estimated for the  
410 RaTS site via (from Emery & Thomson, 2004):

411

$$412 \quad r = \frac{NH}{|f|} \quad (3)$$

413

414 where a water depth of  $H = 520\text{m}$  and a buoyancy frequency of  $N = 2.1 \times 10^{-4} \text{ s}^{-1}$   
415 (which is the maximum value observed within UCDW) yields  $r = 8\text{km}$ . The RaTS site  
416 lies  $\sim 2\text{km}$  from the NE coast of Ryder Bay, and is, therefore, well within one internal  
417 Rossby radius of the coast, whereas the MT mooring lies  $\sim 15\text{km}$ , more than an  
418 internal Rossby radius, from the nearest coastline.

419

420 When an upwelled density structure intersects the surface as an upwelling front, this  
421 front can be driven arbitrarily far offshore by sustained winds (Allen et al., 1995;

422 Austin & Lentz, 2002), so the scale of upwelling influence is no longer set by the  
423 internal Rossby radius. In the present case, it is presumed that upwelling influence  
424 does remain within an internal Rossby radius of the coast for a number of reasons: we  
425 consider temperature levels that are in excess of 115 m deep at the mooring sites,  
426 winds that are highly variable, and an upwelling response that is expected to vary  
427 greatly depending on the local orientation of the coastline. In this setting, it seems  
428 unlikely that upwelling would be sufficiently sustained to bring these isotherms to the  
429 surface nearshore.

430

431 The lack of a clear upwelling signal at MT may be explained in two ways: (1) the  
432 upwelling influence is trapped within an internal Rossby radius of the coastline, and  
433 so does not extend to MT; (2) winds at Rothera are known to differ from those in  
434 other areas of Marguerite Bay (Beardsley et al., 2004), so the correlation of  
435 temperature records from the RaTS site with Rothera winds may suggest that this  
436 upwelling behaviour is a relatively local phenomenon, which cannot therefore be  
437 expected to influence localities such as MT. Further investigation of this spatial  
438 variability would require data from several locations around Marguerite Bay.

439

440 The temporal variability of the quasi-periodic fluctuations is best investigated by  
441 comparison of the total variance,  $\sigma^2$ , over the 2-7 day period for each temperature  
442 sensor (Figure 9) [**insert Figure 9 here**].  $\sigma^2$  of 114-day time series, limited by the  
443 length of deployment 3, is shown for the ice-free and ice-covered seasons of each  
444 RaTS deployment, and values for the two seasons from the different deployments are  
445 compared in Table 4 [**insert Table 4 here**]. In the shallowest two instruments,  $\sigma^2$  is  
446 ~3-4 times as large during the ice-free season as in the presence of ice for both

447 deployments 1 and 2. The difference in  $\sigma^2$  between the ice-free and ice-covered  
448 seasons becomes less pronounced in the deeper instruments during deployment 1, but  
449 remains at a factor of  $\sim 3$ -4 during deployment 2 at all depths. Values from the ice-free  
450 season of deployment 2 are  $\sim 2$ -8 times larger than those of deployments 1 and 3,  
451 whilst during the ice-covered season, values of  $\sigma^2$  from deployment 2 are  $\sim 2$ -3 times  
452 larger than those from deployment 1.

453

454 Coastal upwelling involves both vertical and horizontal motion of the water column,  
455 thus the fluctuations observed at the RaTS site can be expected to arise from both  
456 vertical and lateral temperature gradients. Whilst our data from just two locations are  
457 not sufficient to fully determine the relative importance of horizontal and vertical  
458 water motions in generating the temperature fluctuations, it is possible to estimate the  
459 magnitude of the vertical perturbations of the water column that would be required to  
460 generate the observed fluctuations, thereby providing a realistic upper limit for the  
461 amplitude of the coastal upwelling response. The depth perturbation,  $D'$ , is calculated  
462 from the representative temperature gradient,  $\partial T_{CTD} / \partial z$ , at depth  $z$ , and the magnitude  
463 of the temperature fluctuation,  $T'_m$ , measured at the mooring:

464

$$465 \quad D' = \frac{T'_m}{\partial T_{CTD} / \partial z} \quad (4)$$

466

467 such that a typical temperature perturbation of  $0.3^\circ\text{C}$  at 200m (during the ice-free  
468 season), with an average temperature gradient of  $0.011^\circ\text{C}/\text{m}$  over the depth range 195-  
469 205m, yields  $D' = 27\text{m}$ . Deeper sensors experience smaller temperature

470 perturbations, but the associated temperature gradients are also smaller, so values of  
471  $D'$  are comparable between the different depths.

472

473 In summary, the quasi-periodic fluctuations observed at the RaTS site are a  
474 manifestation of coastal upwelling (downwelling) leading to a temperature increase  
475 (decrease) within the modified UCDW below  $\sim 200\text{m}$  depth. These oscillations are  
476 primarily driven by NW-SE-ward winds that induce upwelling/downwelling along the  
477 NE coast of Ryder Bay,  $\sim 2\text{km}$  from the RaTS site. The ocean's response to the wind  
478 forcing has the potential to generate vertical perturbations of the water column of the  
479 order of several metres to a few tens of metres, and is damped in the presence of pack  
480 ice.

481

## 482 ***4.2 Internal tides***

483

### 484 *4.2.1 Quantification of the barotropic tide*

485 When considering internal tides using subsurface measurements, it is important to be  
486 able to distinguish, and quantify the influence of, the barotropic tide. Here we use the  
487 AntPen04.01 tidal model (Padman, unpublished; [www.esr.org/ptm\\_index](http://www.esr.org/ptm_index)) to estimate  
488 barotropic tides at both moorings locations. The tides in this region are relatively  
489 small, with velocities of  $\leq 3.24\text{cms}^{-1}$  at the RaTS site and  $\leq 0.59\text{cms}^{-1}$  at MT for the  
490 dominant diurnal (O1, K1) and semidiurnal (M2, S2) constituents (see Table 5)  
491 **[insert Table 5 here]**. At the RaTS site, the velocities of the semidiurnal tides are  
492 roughly twice those of the diurnal tides. The M2 and S2 semidiurnal tides, and the O1  
493 diurnal tide, are dominated by the northward component of flow, whilst the K1  
494 diurnal tide is dominated by the eastward component of flow. In contrast, the tidal

495 energy is more evenly distributed between the diurnal and semidiurnal constituents at  
496 MT, and all constituents detailed here are dominated by the eastward component of  
497 flow, although this dominance is weaker in the S2 and K1 tides.

498

499 As can be seen on Figure 1, the RaTS site is located in an elongated basin oriented  
500 roughly E-W, whilst the MT site lies in a trough running NE-SW. Thus, the tidal  
501 energy available for the generation of baroclinic tides is likely to differ between the  
502 two sites, not only due to differences in the barotropic forcing, but also due to the  
503 respective orientations of the barotropic tides relative to the seabed topography.

504

#### 505 *4.2.2 Internal tides in the moored velocity records*

506 Spectra of velocity data using 112-day time series from the moored upward-looking  
507 ADCPs at both mooring sites clearly show energy at tidal frequencies (Figure 10)  
508 **[insert Figure 10 here]**. Spectra from the RaTS site show relatively strong diurnal  
509 tides in eastward velocity ( $u$ ), whilst the semidiurnal tides are virtually absent, despite  
510 the stronger semidiurnal barotropic forcing detailed in Table 5. All tidal signals in  
511 northward velocity ( $v$ ) are weak, despite stronger barotropic forcing in  $v$  than  $u$  for the  
512 M2, S2 and O1 constituents. Both seasonal and interannual variability are observed,  
513 with stronger tidal signatures during the ice-free season, and lower tidally-induced  
514 variance during deployment 3 compared with the other deployments. During the ice-  
515 free season, distinct changes in the strength of the diurnal tidal peaks are observed  
516 with depth, with PSD( $u$ ) from all three deployments showing a distinctive pattern of  
517 relatively high PSD close to the surface and below  $\sim 90\text{m}$ , and a band of low values  
518 centred at  $\sim 50\text{m}$ . This is highlighted in Figure 11 **[insert Figure 11 here]**, which  
519 shows spectra and confidence intervals for  $u$  and  $v$  at selected depths.

520

521 At MT, the energy at diurnal frequencies is comparable to that at the RaTS site, whilst  
522 that at semidiurnal frequencies is significantly higher, despite the diurnal barotropic  
523 forcing being comparable to the M2 semidiurnal forcing. The energy at the  
524 semidiurnal frequencies is likely subject to contributions from the observed strong,  
525 near-inertial energy ( $f$  is very close to the frequencies of the semidiurnal tides at this  
526 latitude). However, non-tidal near-inertial currents would be expected to generate a  
527 broad peak in PSD, whereas the M2 and S2 peaks are well defined, indicating that the  
528 semidiurnal tidal energy is indeed strong compared with the diurnal energy. The  
529 diurnal tides also show slightly higher flow in  $v$  than  $u$ , despite marginally stronger  
530 barotropic forcing in the eastward component of flow. The energy associated with the  
531 O1, K1 and M2 tidal frequencies changes with depth, particularly during the ice-free  
532 season, where they decrease to roughly zero between 50 and 100m, but there is no  
533 increase in energy at depth analogous to that observed at the RaTS site. Selected  
534 spectra (and confidence intervals) from MT are also shown in Figure 11.

535

536 To summarise, velocity data recorded at the two mooring sites show tidal signals that  
537 differ from both their respective barotropic forcings and from each other, and the  
538 strength of the tidal signals changes with depth at both mooring sites. The particularly  
539 strong semidiurnal energy at MT is likely to be influenced by near-inertial currents of  
540 non-tidal origin, with particularly strong semidiurnal tidal currents also present.

541 During the ice-free period, other frequencies (from  $\sim 0.5$  to  $2.0$  cpd) also show  
542 surface-intensified energies at MT, and their absence during the ice-covered periods is  
543 strongly suggestive of atmospheric processes being responsible. (This range of  
544 frequencies includes the diurnal tidal band, explaining the surface-intensification of

545 diurnal tidal energy during the ice-free months at MT). In contrast, the RaTS site does  
546 not experience significant near-inertial energy, and whilst there is evidence of higher  
547 energies in the near-surface layers during the ice-free months, the observed depth-  
548 dependence of the diurnal tidal energy cannot be explained solely by atmospheric  
549 forcing covering a range of frequencies that includes the diurnal band. In particular,  
550 the energy at diurnal frequencies does not consistently decrease away from the  
551 surface, but instead shows a relative minimum in energy at around 50m. This is  
552 consistent with the presence of internal (baroclinic) tides at the RaTS site.

553

554 The tidal currents show distinct interannual variability and are generally reduced  
555 during the ice-covered season, which can be attributed in part to temporal changes in  
556 stratification (Figure 2). However, both seasonal and interannual changes in  $N$  are of  
557 the same order of magnitude ( $\sim 10^{-3} \text{ s}^{-1}$ ), yet seasonal variability in PSD is clearly far  
558 stronger than interannual variability, so the observed changes cannot be attributed to  
559 variability in  $N$  alone. Given that the barotropic forcing is not expected to show strong  
560 temporal variability, the decrease in tidal currents in the presence of ice indicates the  
561 existence of a potentially important relationship between tides and sea ice, which is  
562 worthy of further investigation. Another likely influence upon baroclinic tidal flow is  
563 low frequency current variability (Wallace, 2007), which, by altering the background  
564 density field and introducing background shears, can influence the pathways along  
565 which internal wave energy travels, and thus the manner in which it interacts with  
566 bathymetry (Sherwin & Taylor, 1990).

567

568 To confirm the presence of internal tides we conducted harmonic analysis of ADCP  
569 current data using the Matlab package T\_TIDE (Pawlowicz et al., 2002). Figure 12



570 **[insert Figure 12 here]** shows profiles of tidal phase extracted for the O1, K1, M2  
571 and S2 tides at the RaTS site and MT. Phase shifts of  $180^\circ$ , characteristic of internal  
572 tides (Gill, 1982), are observed at the RaTS site, whilst no such phase shifts occur at  
573 MT. However, it is necessary to consider that the MT ADCP samples the upper  
574  $\sim 100\text{m}$  of a water column that is  $>800\text{m}$  deep, so the lack of phase change measured  
575 at this location does not necessarily indicate the absence of internal tides. The RaTS  
576 data show a larger number of  $180^\circ$  phase changes for the semidiurnal than the diurnal  
577 constituents, but due to the low tidal energy at the semidiurnal frequencies at this site,  
578 and the associated difficulties of relating phase information to the observed  
579 variability, the following discussion will concentrate upon the diurnal tides during the  
580 ice-free season, and in particular the eastward component of flow.

581

582 The phase profiles at the RaTS site highlight three primary regimes of variability over  
583 the depth profiles: (1) relatively high variability above  $\sim 40\text{m}$ , characterised by  $180^\circ$   
584 phase shifts in O1 and K1 of deployment 2, and O1 of deployment 3; (2) low  
585 variability between  $\sim 40$  and  $\sim 100\text{-}120\text{m}$ , characterised by virtually constant phase;  
586 and (3) high variability below  $\sim 100\text{-}120\text{m}$ , characterised by between one and ten  $180^\circ$   
587 phase changes. These phase changes indicate regions of high shear and correspond  
588 well with the near-surface and deep regions of high energy shown in  $u$  in Figure 10,  
589 and/or the transitions between regions of high and low energy, whilst the relatively  
590 stable phase profile between  $\sim 40$  and  $\sim 100\text{-}120\text{m}$  corresponds well with the low  
591 energy observed at these depths. However, the relatively constant phase throughout  
592 the shallow water column for O1 and K1 of deployment 1, and K1 of deployment 3,  
593 indicates that relatively large changes in PSD with depth need not be associated with  
594 current reversals.

595

596 Profiles of diurnal tidal amplitude are also in good agreement with the results from the  
597 RaTS PSD analysis (Figure 13a-c) [**insert Figure 13 here**], with the lowest  
598 amplitudes observed where PSD is lowest. This change in tidal amplitude with depth  
599 is also indicative of baroclinic tides (a barotropic tide should not show such  
600 variability), confirming their importance at the RaTS site. Amplitude profiles from  
601 MT (Figure 13d) also show a decrease with depth, particularly at the semidiurnal  
602 frequencies, which is again consistent with the observed patterns in PSD. This  
603 indicates that, even though no phase change is observed at this location, the site is  
604 influenced by internal tides.

605

#### 606 *4.2.3 Generations sites of internal tides*

607 The inconsistencies between the expected and observed relative strengths of the  
608 eastward and northward components of tidal flow at the RaTS site suggest that the  
609 orientation of the flow with respect to seabed topography is important. The location of  
610 Marguerite Bay poleward of the critical latitude for diurnal internal tides, but  
611 equatorward of that for semidiurnal internal tides, implies that the superinertial  
612 semidiurnal signal should be allowed to propagate freely (although it may be locally  
613 generated), whilst we expect the subinertial diurnal internal tide to be generated in the  
614 region of our moorings or to have propagated along the coastline or local bathymetric  
615 slope with an offshore or off-slope horizontal length scale of the order of the internal  
616 Rossby radius. The strong diurnal internal signal at the RaTS site is thus consistent  
617 with its proximity to the coast.

618

619 Internal tides have been observed in the Arctic (e.g. Konyaev et al., 2000; Morozov et  
620 al., 2003) and around the margins of Antarctica (e.g. Foldvik et al., 1990; Levine et  
621 al., 1997; Albrecht et al., 2006), and both models (e.g. Morozov & Pisarev, 2002;  
622 Padman et al., 2006) and observational work (e.g. Albrecht et al., 2006) suggest that  
623 the interaction of barotropic flows with seabed topography is an important process in  
624 the generation and propagation of internal tides. In order to identify potential  
625 generation sites in the vicinity of the two mooring sites we derive the internal tidal  
626 forcing function,  $F$ , after Sherwin (1988):

627

$$628 \quad F = \frac{izQN^2}{\omega} \nabla \left( \frac{1}{H} \right) \quad (5)$$

629

630 where  $Q$  is the tidal flow (defined as  $uH$ ,  $vH$ , where  $u$ ,  $v$  are the eastward and  
631 northward velocities and  $H$  the water depth),  $\omega$  is the frequency of the internal tide,  $z$   
632 is the depth of interest and  $\nabla \left( \frac{1}{H} \right)$  is the horizontal gradient of the inverse of the  
633 water depth. Bathymetry data are from the US SO-GLOBEC program  
634 ([www.whoi.edu/science/PO/so\\_globec/WHOI\\_tech\\_report](http://www.whoi.edu/science/PO/so_globec/WHOI_tech_report)) and are used internally in  
635 AntPen04.01 to calculate  $uH$  and  $vH$  across the regions around each mooring site  
636 marked in Figure 1. The calculation is carried out for both the ice-free and ice-  
637 covered seasons of all years at the RaTS site, but results are shown here for 2006  
638 only. Deployments 1 and 3 show results consistent with those presented here. Average  
639 profiles of  $N$  are calculated for the ice-free and ice-covered seasons from CTD  
640 profiles collected from February-June 2006 and July-November 2006, respectively.  
641 The analysis is carried out for both the K1 and M2 internal tides, in order to permit  
642 comparison of the potential local generation sites for both diurnal and semidiurnal

643 internal tides.  $F^*$  is also calculated for the K1 and M2 tides during the ice-free season  
644 at MT, using a profile of  $N$  derived from a CTD cast carried out at this location during  
645 February 2006. In the absence of winter CTD profiles at this location,  $F^*$  cannot be  
646 calculated for the ice-covered season.

647

648 Figure 14a-d [**insert Figure 14 here**] shows depth-integrated tidal forcing function,  
649  $F^*$ , for the region around the RaTS site marked on Figure 1. For both tidal  
650 constituents, values of  $F^*$  are of the order of 1-2  $\text{Nm}^{-2}$  over much of the domain but  
651 can be  $>50 \text{Nm}^{-2}$  over areas of rugged bathymetry. At MT (Figure 14e-f),  $F^*$  is  
652 generally higher, particularly for K1, with values of  $\sim 10 \text{Nm}^{-2}$  over much of the  
653 region and, again  $>50 \text{Nm}^{-2}$  over areas of rugged bathymetry. These results echo those  
654 of Sherwin (1988) and Sherwin & Taylor (1990), who studied internal tides generated  
655 over the region of the Malin Shelf, north of Ireland. Sherwin & Taylor (1990) derived  
656 the highest values of  $F^*$  ( $\leq 60 \text{Nm}^{-2}$ ) at the continental shelf break and values of  $\sim 10$ -  
657  $20 \text{Nm}^{-2}$  over the continental slope. The results of Sherwin (1988) were similar, with  
658 values of  $F^* \leq 40 \text{Nm}^{-2}$  at the shelf break and, again,  $\sim 10$ - $20 \text{Nm}^{-2}$  over the  
659 continental slope, and he concluded that both regions were important for the  
660 generation of the observed internal tides.

661

662 The similarity of  $F^*$  derived for the Malin Shelf and Marguerite Bay is worthy of  
663 note, given that  $N$  measured on the Malin Shelf was roughly twice that in Marguerite  
664 Bay and the tidal forcing of the North Atlantic is an order of magnitude larger than  
665 that on the WAP (Sherwin 1988). We therefore conclude that the rugged nature of the  
666 WAP bathymetry, as reflected in  $\nabla\left(\frac{1}{H}\right)$ , has the potential to induce relatively strong  
667 baroclinic tides, despite the weak barotropic forcing and weak stratification.

668

669 Potential generation sites for the diurnal internal tide observed at the RaTS site are the  
670 NE coastline and around the small islands to the SW side of Ryder Bay. Values of  $F^*$   
671 are slightly higher over the region for the M2 internal tide due to larger values of  $Q$   
672 (see details of tidal current flow in Table 5), although this is offset in part by the  
673 increase in  $\omega$ , and lower during the ice-covered season for both tidal constituents due  
674 to reduced stratification. However, given the similarities between the four maps, the  
675 influences of  $Q$ ,  $N$  and  $\omega$  are clearly small compared to that of the bathymetry. Maps  
676 of  $F^*$  for the eastward and northward components of flow are not shown separately  
677 here, but  $vH$  accounts for  $\sim 69\%$  of the diurnal  $Q$  and  $\sim 75\%$  of the semidiurnal  $Q$ .  
678 Thus, the observed temporal variability in PSD, the differences between PSD of the  
679 diurnal and semidiurnal constituents, and the marked dominance of  $\text{PSD}(u)$  over  
680  $\text{PSD}(v)$  cannot be solely attributed to differences in internal tide generation sites, or  
681 orientation of the tidal flow with respect to the known bathymetry.

682

683 At MT, most of the potential generation sites are located around the northern and  
684 western margins of the trough in which the mooring lies. The areas of high  $F^*$  ( $>20$   
685  $\text{Nm}^{-2}$ ) are similar for both the diurnal and semidiurnal constituents, but the higher  
686 value of  $\omega$  for the semidiurnal tide leads to a clear decrease in  $F^*$  over much of the  
687 domain. In contrast to the RaTS site,  $uH$  dominates  $Q$ , accounting for  $\sim 61\%$  of the  
688 diurnal  $Q$  and  $\sim 67\%$  of the semidiurnal  $Q$ . Given that  $u$  and  $v$  are similar for K1, this  
689 shows that the orientation of the tidal flow with respect to the topography is an  
690 important factor.

691

692

693 **5. Discussion**

694

695 This study has shown that northern Marguerite Bay is affected by internal tides,  
696 although their nature differs between the nearshore RaTS site and the offshore MT  
697 site. At the RaTS site, energy at the diurnal frequencies dominates over the  
698 semidiurnal energy, despite stronger barotropic forcing at semidiurnal frequencies.  
699 The orientation of the tidal flow with respect to seabed topography is also important,  
700 with higher energy observed in the eastward component of tidal flow for both the O1  
701 and K1 internal tides, despite O1 being subject to stronger northward barotropic flow.  
702 An investigation of internal tide generation sites around Ryder Bay also indicates that  
703 the northward component of flow has more potential for generating internal tides, due  
704 to its orientation with respect to bathymetric features. However, observations show  
705 stronger tidal flow in the eastward direction, implying that the relationship between  
706 the forcing and propagation of the internal tides is complex. In addition, the RaTS site  
707 is influenced by quasi-periodic temperature fluctuations that we have shown are due  
708 to local wind-forced coastal upwelling and downwelling.

709

710 At MT, tidal energy is far stronger at the semidiurnal frequencies than the diurnal  
711 frequencies, despite similar barotropic forcing. Atmospherically-forced signals are  
712 observed to contribute to the energy at both the diurnal and semidiurnal frequencies,  
713 but the signatures of the baroclinic tides can still be observed in the upper water  
714 column. Again, the orientation of tidal flow with respect to seabed topography is  
715 important, with the eastward component of flow having the strongest potential for  
716 internal tide generation.

717

718 There are a number of possible explanations for the temporal variability of both the  
719 atmospherically and tidally-forced signals. The most likely are: (1) changes in  
720 stratification, whereby stronger stratification leads to a stronger internal wave signal  
721 due to higher variance at the depth of interest; (2) changes in background vertical  
722 shear arising from low frequency current variability; and (3) changes in sea ice  
723 conditions, which appear to affect tidal flow and have the potential to influence the  
724 atmospherically-forced signal, such that ice thickness, coherence and ridging can  
725 influence the transmission of wind-forcing to the ocean (e.g. Steele et al., 1989;  
726 Andreas et al., 1993; McPhee et al., 1999).

727

728 Considering each of these possibilities in turn:

729

730 (1) Changes in stratification undoubtedly influence the temporal variability of  
731 both the atmospherically-forced and baroclinic tidal flows. However, it has  
732 been demonstrated that neither seasonal nor interannual changes in  
733 stratification can account for all of the variability in either the  
734 atmospherically-forced signal or the internal tides.

735

736 (2) Seasonal and interannual changes in low frequency currents have been  
737 observed in the uppermost 200m of the water column at the RaTS site  
738 (Wallace, 2007) and are likely to account for some of the changes in internal  
739 tidal activity that are not related to stratification. There are, however, currently  
740 insufficient data for a full investigation of this theory.

741

742 (3) The rapid response and decay of the atmospherically-forced signal to the onset  
743 of pack ice clearly indicates that sea ice conditions have an important  
744 influence upon the oscillations. Observations from Rothera Research Station  
745 suggest that the ice was more fragmented during the winter of 2006 than 2005,  
746 which is consistent with the continuation of the (albeit weakened) oscillation  
747 throughout the ice-covered season of 2006. More detailed ice data (including  
748 thickness, degree of ridging etc) are required to assess further the dynamical  
749 role of ice in suppressing atmospherically-forced oscillations. The seasonal  
750 variability in the tidal energy at the RaTS site is likely linked to sea ice  
751 conditions, but the nature of this connection is as yet unclear.

752

## 753 **6. Conclusions**

754

755 We conclude that internal perturbations in northern Marguerite Bay are subject to a  
756 number of influences, including local winds, sea ice, barotropic tides and  
757 stratification. The observed internal wave and coastal upwelling activity may  
758 contribute to vertical mixing and nutrient distribution in Ryder Bay, with potential  
759 consequences for the operation of the local ecosystem; this is thus worthy of further  
760 investigation. The presence of a wind-driven signal beneath the permanent pycnocline  
761 at the RaTS site indicates that the UCDW is, locally at least, subject to some degree of  
762 atmospheric forcing, implying that changes in sea ice cover or atmospheric circulation  
763 could have implications for mixing processes in these deep waters. The absence of the  
764 wind-driven signal at the MT site demonstrates that Ryder Bay is subject to at least  
765 some different forcing mechanisms to those of the more open waters of Marguerite  
766 Bay, as does the difference in the internal tidal signals between the two locations. The



767 RaTS programme is continuing in Ryder Bay, and we are planning to redeploy our  
768 fixed moorings within the next few years, including deployments at other sites within  
769 Marguerite Bay and on the broader WAP shelf. This will allow us to quantify better  
770 the roles of the processes elucidated above, and to assess the local impacts of the  
771 internal waves and coastal upwelling on the marine ecosystem.

772

773

774

775 Acknowledgements

776 We would like to thank personnel at the British Antarctic Survey's Rothera Research  
777 Station, particularly the Marine Assistants and boatmen, without whom the collection  
778 of RaTS CTDs since 1998 would not have been possible. Thanks also to the scientists  
779 and crew aboard the RRS *James Clark Ross* and the RV *Laurence M Gould*, and to  
780 the mooring technicians from the National Oceanography Centre, Southampton, for  
781 all their help and hard work. Many thanks to Bob Beardsley for providing the SO-  
782 GLOBEC data used here, the Proudman Oceanographic Laboratory for the Rothera  
783 tide gauge data and Laurie Padman for the AntPen04.01 model data. Thanks also to  
784 Carlos Moffat and an anonymous reviewer for positive and constructive feedback on  
785 this paper. The Rothera Time Series, Marguerite Bay moorings and Margaret  
786 Wallace's PhD studentship were funded by the Natural Environment Research  
787 Council in the AFI Scheme, grant number NER/S/S/2004/13013.

788

789

790

791

792 References

- 793 Albrecht, N., Vennell, R., Williams, M., Stevens, C., Langhorne, P., Leonard, G. and  
794 Haskell, T., 2006. Observation of sub-inertial internal tides in McMurdo Sound,  
795 Antarctica. *Geophysical Research Letters* 33, L24606, doi:10.1029/2006GL027377.
- 796 Allen, J. S., Newberger, P.A., Federiuk, J., 1995. Upwelling circulation on the Oregon  
797 continental shelf. Part I: Response to idealized forcing. *Journal of Physical*  
798 *Oceanography* 25, 1843-1866.
- 799 Andreas, E. L., Lange, M.A., Ackley, S.F., Wadhams, P., 1993. Roughness of  
800 Weddell sea ice and estimates of the air-ice drag coefficient. *Journal of Geophysical*  
801 *Research* 98 (C7), 12439-12452.
- 802 Austin, J. A. and Barth, J.A., 2002. Variation in the position of the upwelling front on  
803 the Oregon shelf. *Journal of Geophysical Research* 107 (C11), 3180,  
804 doi:10.1029/2001JC000858.
- 805 Austin, J. A., Lentz, S.J., 2002. The inner shelf response to wind-driven upwelling  
806 and downwelling. *Journal of Physical Oceanography* 32, 2171-2193.
- 807 Beardsley, R. C., Limeburner, R. and Owens, W.B., 2004. Drifter measurements of  
808 surface currents near Marguerite Bay on the western Antarctic Peninsula shelf during  
809 austral summer and fall, 2001 and 2002. *Deep-Sea Research II* 51, 1947-1964.
- 810 Dinniman, M. S. and Klinck, J.M., 2004. A model study of circulation and cross-shelf  
811 exchange on the west Antarctic Peninsula continental shelf. *Deep-Sea Research II* 51,  
812 2003-2022.
- 813 Clarke, A., Meredith, M.P., Wallace, M.I., Brandon, M.A. and Thomas, D.N., in  
814 press. Seasonal and interannual variability in temperature, chlorophyll and  
815 macronutrients in Ryder Bay, northern Marguerite Bay, Antarctica. *Deep-Sea*  
816 *Research II*, PAL-LTER Special Issue.

817 Costa, D.P. and Crocker, D.E., 1996. Marine mammals of the Southern Ocean. In:  
818 Ross, R.M., Hofmann, E.E., Quetin, L.B. (Eds.), Foundations for Ecological Research  
819 West of the Antarctic Peninsula, Antarctic Research Series 70. AGU, Washington,  
820 D.C., pp. 287-301.

821 Dinniman, M. S., Klinck, J.M., 2004. A model study of circulation and cross-shelf  
822 exchange on the west Antarctic Peninsula continental shelf. Deep-Sea Research II 51,  
823 2003-2022.

824 Emery, W. J. and Thomson, R.E., 2004. Data Analysis Methods in Physical  
825 Oceanography. Elsevier, Amsterdam.

826 Foldvik, A., Middleton, J. and Foster, T., 1990. The tides of the southern Weddell  
827 Sea. Deep-Sea Research 97, 1345-1362.

828 Fraser, W.R. and Trivelpiece, W.Z., 1996. Factors controlling the distribution of  
829 seabirds: winter-summer heterogeneity in the distribution of Adélie penguin  
830 populations. In: Ross, R.M., Hofmann, E.E., Quetin, L.B. (Eds.), Foundations for  
831 Ecological Research West of the Antarctic Peninsula, Antarctic Research Series 70.  
832 AGU, Washington, D.C., pp. 257-272.

833 Gill, A. E., 1982. Atmosphere-Ocean Dynamics. International Geophysics Series 30.  
834 Academic Press, San Diego, California.

835 Gregg, M. C., 1987. Diapycnal mixing in the thermocline: a review. Journal of  
836 Geophysical Research 92 (C5), 5249-5286.

837 Halpern, D., 1976. Structure of a coastal upwelling event observed off Oregon during  
838 July 1973. Deep-Sea Research 23, 495-508.

839 Hofmann, E. E. and Klinck, J.M., 1998. Thermohaline variability of the waters  
840 overlying the West Antarctic Peninsula Continental Shelf. In: Jacobs, S., Weiss, R.

841 (Eds.), *Oceans, Ice and Atmosphere: Interactions at the Antarctic Continental Margin*,  
842 *Antarctic Research Series 75*. AGU, Washington, D.C., pp. 67-81.

843 Howard, S. L., Hyatt, J., Padman, L., 2004. Mixing in the pycnocline over the western  
844 Antarctic Peninsula shelf during Southern Ocean GLOBEC. *Deep-Sea Research II* 51,  
845 1965-1979.

846 Hyatt, J., Visbeck, M., Beardsley, R., Owens, W.B., 2008. Measurements of sea ice  
847 properties using a moored upward-looking acoustic Doppler current profiler (ADCP).  
848 *Deep-Sea Research II* 55, 351-364.

849 Intergovernmental Oceanographic Commission of UNESCO (IOC), 2006. Manual on  
850 sea-level measurements and interpretation, volume IV: an update to 2006. IOC  
851 Manuals and Guides IV (14), JCOMM Technical Report No. 31; WMO/TD. No.1339,  
852 56 pp.

853 Klinck, J. M., 1998. Heat and salt changes on the continental shelf west of the  
854 Antarctic peninsula between January 1993 and January 1994. *Journal of Geophysical*  
855 *Research* 103 (C4), 7617-7636.

856 Klinck, J. M., Hofmann, E.E., Beardsley, R.C., Salihoglu, B. and Howard, S., 2004.  
857 Water-mass properties and circulation on the west Antarctic Peninsula Continental  
858 Shelf in Austral Fall and Winter 2001. *Deep-Sea Research II* 51, 1925-1946.

859 Koentopp, M., Eisen, O., Kottmeier, C., Padman, L., Lemke, P., 2005. Influence of  
860 tides on sea ice in the Weddell Sea: investigations with a high-resolution dynamic-  
861 thermodynamic sea ice model. *Journal of Geophysical Research* 110 (C02014), 137-  
862 158.

863 Konyaev, K. V., 2000. Internal tide at the critical latitude. *Izvestiya, Atmospheric and*  
864 *Oceanic Physics* 36 (3), 363-375.

865 Konyaev, K. V., Plueddemann, A. and Sabinin, K.D., 2000. Internal tide on the  
866 Yermak Plateau in the Arctic Ocean. *Izvestiya, Atmospheric and Oceanic Physics* 36  
867 (4), 542-552.

868 Kowalik, Z. and Proshutinsky, A.Y., 1994. The Arctic Ocean tides. In: Johansse,  
869 O.M., Muench, R.D., Overland, J.E. (Eds.), *The Polar Oceans and their role in*  
870 *shaping the Global Environment*, Geophysical Monograph 85. AGU, Washington,  
871 D.C., pp. 137-158.

872 LeBlond, P., Mysak, L.A., 1978. *Waves in the ocean*. Elsevier Oceanographic Series  
873 20. Elsevier, Amsterdam.

874 Levine, M. D., Padman, L., Muench, R.D. and Morison, J.H., 1997. Internal waves  
875 and tides in the western Weddell Sea: Observations from Ice Station Weddell. *Journal*  
876 *of Geophysical Research* 102 (C1), 1073-1089.

877 Mackinnon, J. A. and Gregg, M.C., 2005. Spring mixing: turbulence and internal  
878 waves during restratification on the New England shelf. *Journal of Physical*  
879 *Oceanography* 35, 2425-2443.

880 Martinson, D.G., Stammerjohn, S.E., Iannuzzi, R.A. and Smith, R.C. in press. Palmer,  
881 Antarctica, Long-term Ecological Research Program first twelve years: Physical  
882 oceanography, spatio-temporal variability. *Deep-Sea Research II*, PAL-LTER Special  
883 Issue.

884 McPhee, M. G., Kottmeier, C., Morison, J.H., 1999. Ocean heat flux in the central  
885 Weddell Sea during winter. *Journal of Physical Oceanography* 29, 1166-1179.

886 Meredith, M. P., Renfrew, I.A., Clarke, A., King, J.C. and Brandon, M.A., 2004.  
887 Impact of the 1997/98 ENSO on upper ocean characteristics in Marguerite Bay,  
888 western Antarctic Peninsula. *Journal of Geophysical Research* 109, 9013-9032.

889 Mitchum, G. T., Clarke, A.J., 1986. The frictional nearshore response to forcing by  
890 synoptic scale winds. *Journal of Physical Oceanography* 16, 934-946.

891 Morozov, E. G. and Pisarev, S.V., 2002. Internal tides at the Arctic latitudes  
892 (numerical experiments). *Oceanology* 42 (2), 165-173.

893 Morozov, E. G., Pisarev, S.V., Neiman, V.G. and Erofeeva, S.Y., 2003. Internal tidal  
894 waves in the Barents Sea. *Doklady Earth Sciences* 393 (8), 686-688 (translated from  
895 Russian).

896 Muench, R. D., Padman, L., Howard, S.L., Fahrbach, E., 2002. Upper ocean  
897 diapycnal mixing in the northwestern Weddell Sea. *Deep-Sea Research II* 49, 4843-  
898 4861.

899 Munk, W. and Wunsch, C., 1998. Abyssal recipes II: energetics of tidal and wind  
900 mixing. *Deep-Sea Research I* 45, 1977-2010.

901 New, A. L., 1988. Internal tidal mixing in the Bay of Biscay. *Deep Sea Research* 35  
902 (5), 691-709.

903 New, A. L. and Pingree, R.D., 1990. Evidence for internal tidal mixing near the shelf  
904 break in the Bay of Biscay. *Deep Sea Research* 37 (12), 1783-1803.

905 Ostrovsky, I., Yacobi, Y.Z., Walline, P. and Kalikhman, I., 1996. Seiche-induced  
906 mixing: Its impact on lake productivity. *Limnology and Oceanography* 41 (2), 323-  
907 332.

908 Padman, L., Fricker, H. A., Coleman, R., Howard, S., Erofeeva, L., 2002. A new tide  
909 model for the Antarctic ice shelves and seas. *Annals of Glaciology* 34, 247-254.

910 Padman, L., Howard, S., Muench, R., 2006. Internal tide generation along the South  
911 Scotia Ridge. *Deep Sea Research II: Topical Studies in Oceanography* 53, 157-171.

912 Pawlowicz, R., Beardsley, B. and Lentz, S., 2002. Classical tidal harmonic analysis  
913 including error estimates in MATLAB using T\_TIDE. *Computers and Geoscience*,  
914 28, 929-937.

915 Polzin, K. L., Toole, J.M., Ledwell, J.R. and Schmitt, R.W., 1997. Spatial variability  
916 of turbulent mixing in the abyssal ocean. *Science* 276, 93-96.

917 Pond, S. and Pickard, G.L., 1983. *Introductory dynamical oceanography*, 2<sup>nd</sup> Edition.  
918 Pergamon Press, Oxford.

919 Rippeth, T. P. and Inall, M.E., 2002. Observations of the internal tide and associated  
920 mixing across the Malin Shelf. *Journal of Geophysical Research* 107 (C4), 8687-  
921 8705.

922 Ross, R.M., Quetin, L.B. and Lascara, C.M. (1996a). Distribution of Antarctic krill  
923 and dominant zooplankton west of the Antarctic Peninsula. In: Ross, R.M., Hofmann,  
924 E.E., Quetin, L.B. (Eds.), *Foundations for Ecological Research West of the Antarctic*  
925 *Peninsula*, Antarctic Research Series 70. AGU, Washington, D.C., pp. 199-217.

926 Ross, R.M., Hofmann, E.E. and Quetin, L.B., editors, 1996b. *Foundations for*  
927 *ecological research west of the Antarctic Peninsula*, Antarctic Research Series 70.  
928 AGU, Washington, D.C., 448 pp.

929 Sherwin, T. J., 1988. Analysis of an internal tide observed on the Malin Shelf, north  
930 of Ireland. *Journal of Physical Oceanography* 18, 1035-1050.

931 Sherwin, T.J. and Taylor, N.K., 1990. Numerical investigations of linear internal tide  
932 generation in the Rockall Trough. *Deep-Sea Research* 37 (10), 1595-1618.

933 Simpson, J. H. and Rippeth, T., 1993. The Clyde Sea: a model of the seasonal cycle of  
934 stratification and mixing. *Estuarine Coastal Shelf Science* 37, 129-144.

935 Small, L. F., Menzies, D.W., 1981. Patterns of primary productivity and biomass in a  
936 coastal upwelling region. *Deep Sea Research* 28A, 123-149.

937 Smith, D. A. and Klinck, J.M., 2002. Water properties on the west Antarctic  
938 Peninsula continental shelf: a model study of effects of surface fluxes and sea ice.  
939 Deep-Sea Research II 49, 4863-4886.

940 Smith, D. A., Hofmann, E.E., Klinck, J.M., Lascara, C.M., 1999. Hydrography and  
941 circulation of the West Antarctic Peninsula Continental Shelf. Deep-Sea Research I  
942 46, 925-949.

943 Steele, M., Morison, J.H., Untersteiner, N., 1989. The partition of air-ice-ocean  
944 momentum exchange as a function of ice concentration, floe size and draft. Journal of  
945 Geophysical Research 94 (C9), 12739-12750.

946 Stigebrandt, A., 1976. Vertical diffusion driven by internal waves in a sill fjord.  
947 Journal of Physical Oceanography 6, 486-495.

948 Stigebrandt, A., 1999. Baroclinic wave drag and barotropic to baroclinic energy  
949 transfer at sills as evidence by tidal retardation, seiche damping and diapycnal mixing  
950 in fjords. In: Muller, P., Henderson, D. (Eds.), Dynamics of Internal Gravity Waves  
951 II, Proc. Aha Huliko' a Hawaiian Winter Workshop. University of Hawaii, Honolulu,  
952 Hawaii, pp. 73-82.

953 Stigebrandt, A. and Aure, J., 1989. Vertical mixing in basin waters of fjords. Journal  
954 of Physical Oceanography 19, 917-926.

955 Toole, J. M., 1981. Sea ice, winter convection and temperature minimum layer in the  
956 Southern Ocean. Journal of Geophysical Research 86 (C9), 8037-8047.

957 Trenberth, K. E., 1984. Signal Versus Noise in the Southern Oscillation. Monthly  
958 Weather Review 112 (2), 326-332.

959 Visbeck, M. and Fischer, J., 1995. Sea-Surface Conditions Remotely-Sensed by  
960 Upward-Looking ADCPs. Journal of Atmospheric and Oceanic Technology 12 (1),  
961 141-149.



962 Wallace, M.I., 2007. Ocean circulation, properties and variability in Marguerite Bay,  
963 west Antarctic Peninsula. PhD Thesis, The Open University, Milton Keynes, UK,  
964 unpublished.

965 Winant, C. D., 1980. Downwelling over the southern California shelf. *Journal of*  
966 *Physical Oceanography* 10, 791-799.

967 Woodworth, P. L., Vassie, J.M., Spencer, R. and Smith, D.E., 1996. Precise datum  
968 control for pressure tide gauges. *Marine Geodesy* 19, 1-20.

969 Woodworth, P.L., Hughes, C.W., Blackman, D.L., Stepanov, V., Holgate, S., Foden,  
970 P.R., Mack, S., Hargreaves, G.W., Meredith, M.P., Milinevsky, G. and Fierro  
971 Contreras, J.J., 2006. Antarctic Peninsula sea levels: a real time system for monitoring  
972 Drake Passage transport. *Antarctic Science* 18 (3), 429-436.

973

974

975

976

977

978

979

980

981

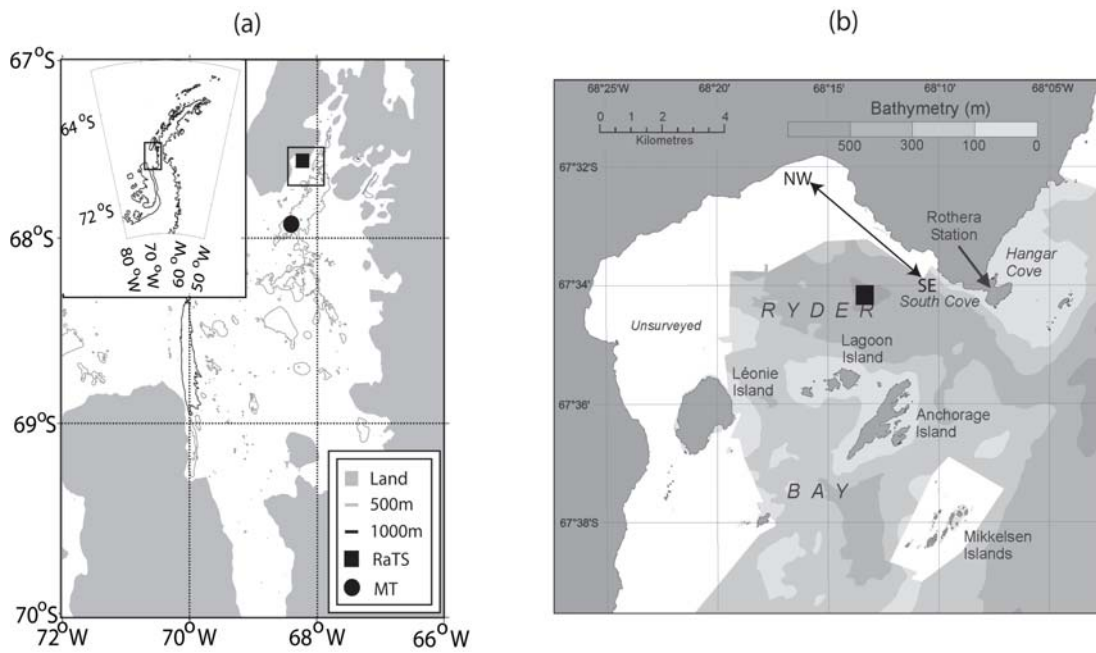
982

983

984

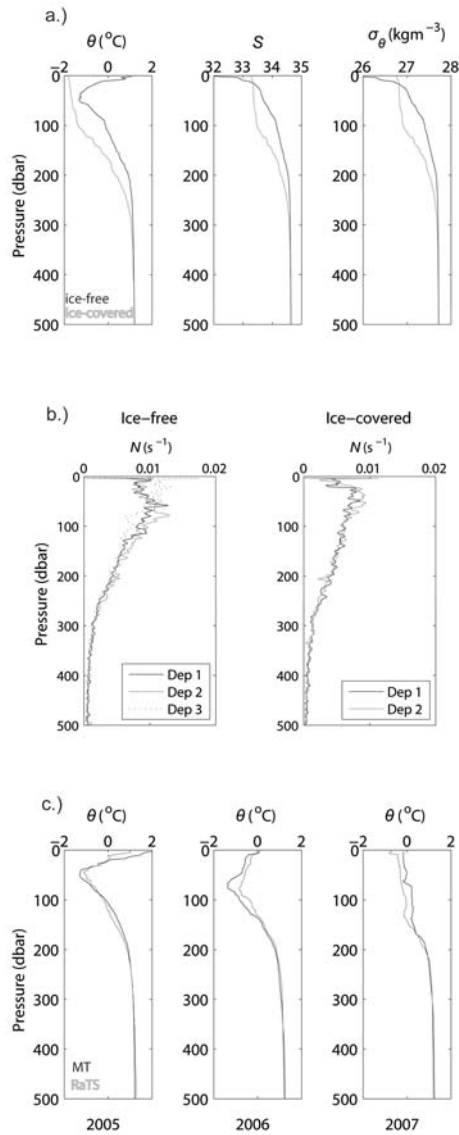
985

986



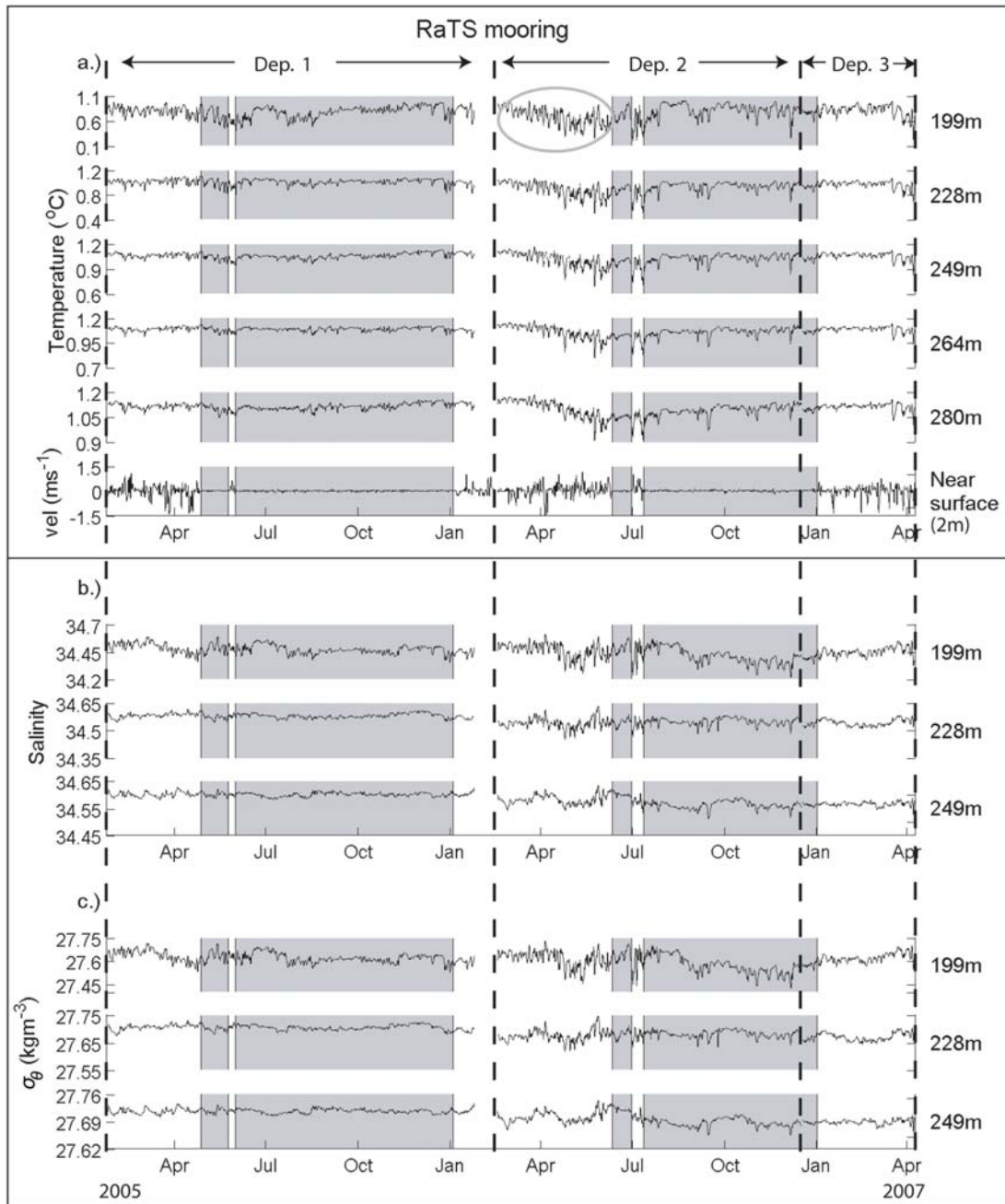
987  
 988  
 989  
 990  
 991  
 992  
 993  
 994  
 995  
 996  
 997

Figure 1: (a) Marguerite Bay (black box on inset of the Antarctic Peninsula). The coast, 1000m contour and 500m contours are delineated by thick grey, thin black and thin grey lines, respectively. The RaTS mooring (black square) and the MT mooring (black circle) are shown, and thick black lines delineate areas surrounding the moorings examined in Section 4.2. The area surrounding the RaTS mooring is expanded in (b), courtesy of the Mapping and Geographic Information Centre (MAGIC), BAS. The RaTS site is marked with a black square. The black, double-headed arrow shows the NW-SE wind orientation to which Section 4.1 refers.



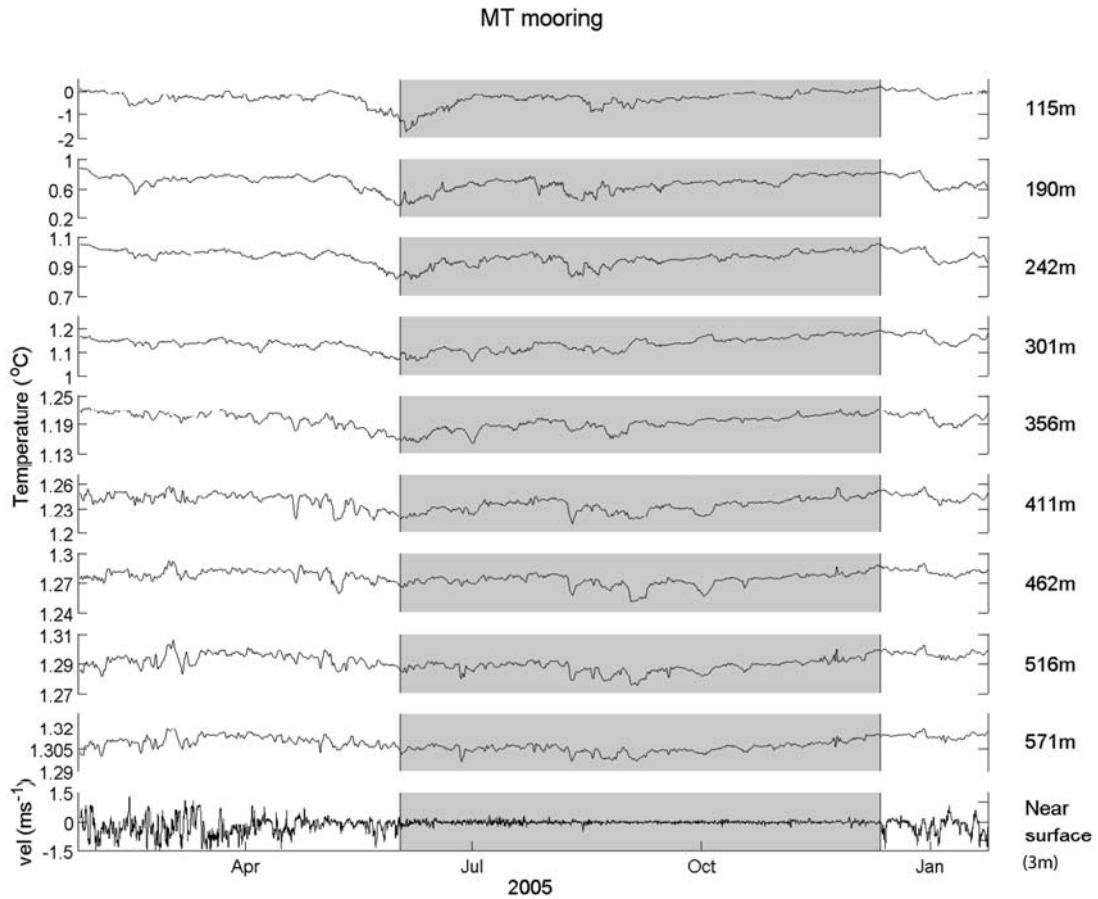
998  
999

1000 Figure 2: (a) Typical profiles of potential temperature, salinity and potential density  
 1001 anomaly from the RaTS site for the ice-free (black) and ice-covered (grey) seasons;  
 1002 (b) mean buoyancy frequency profiles for the ice-free and ice-covered seasons at the  
 1003 RaTS site (Dep 1, 2 and 3 refer to the deployment); and (c) comparison of potential  
 1004 temperature profiles from the RaTS site (grey) and MT (black) from January 2005,  
 1005 February 2006 and April 2007.  
 1006



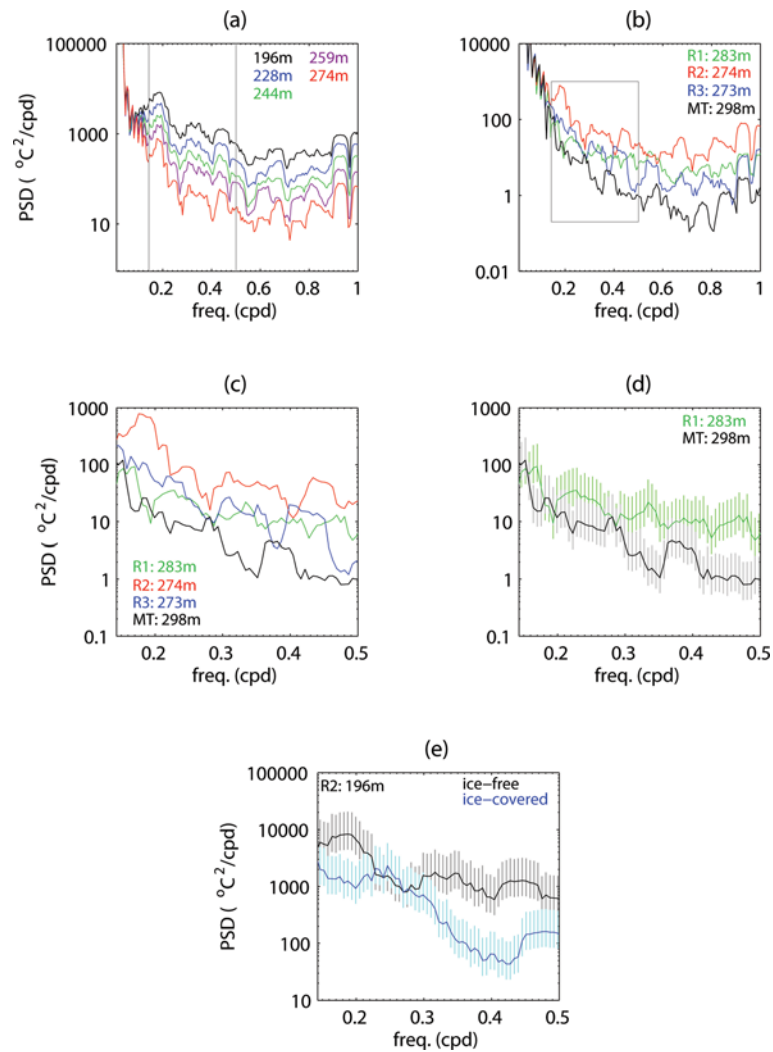
1007  
 1008  
 1009  
 1010  
 1011  
 1012  
 1013  
 1014  
 1015  
 1016  
 1017  
 1018  
 1019

Figure 3: (a) Temperature,  $T$ , (b) salinity,  $S$ , and (c) potential density anomaly,  $\sigma_{\theta}$ , time series from the RaTS site. Horizontal velocity data from the bin of the upward-looking ADCP closest to the surface are included at the bottom of panel (a). All time series are filtered using a 26-hour Butterworth lowpass filter to remove tidal and higher frequency variability. The velocity data are used to identify periods of ice cover (velocity variance is reduced in the presence of ice). Ice presence is shaded in grey on each panel. The three deployments are bordered by black dashed lines and the mean depth of each time series over the three deployments is noted to the right of each trace. The grey oval marks an example of the 2-7 day quasi-periodic signal examined in Section 4.1.



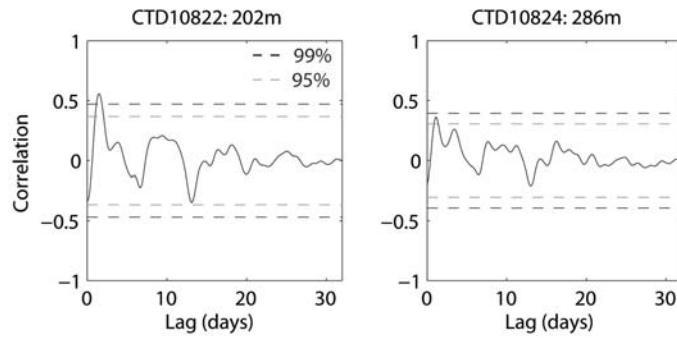
1020  
 1021  
 1022  
 1023  
 1024  
 1025  
 1026  
 1027  
 1028  
 1029

Figure 4: Temperature time series from the MT site. Horizontal velocity data from the bin of the upward-looking ADCP closest to the surface are included at the bottom of the panel. All time series are filtered using a 26-hour Butterworth lowpass filter to remove tidal and higher frequency variability. The velocity data are used to identify periods of ice cover (velocity variance is reduced in the presence of ice). Ice presence is shaded in grey on each panel. The depth of each time series is noted to the right of each trace.



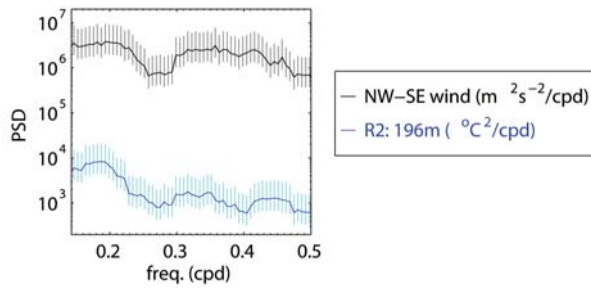
1030  
 1031  
 1032  
 1033  
 1034  
 1035  
 1036  
 1037  
 1038  
 1039  
 1040  
 1041  
 1042  
 1043  
 1044

Figure 5: Log-linear plots of power spectral density (PSD) for 126-day temperature time series: (a) for all sensors from RaTS deployment 2 during the ice-free season; (b) 298m at MT, and 283m, 274m and 273m for RaTS deployments 1-3, respectively, for the ice-free season. The grey square marks the 2-7 day period, which is expanded in (c) for the four time series; (d) shows spectra from the MT mooring (black, 298m) and RaTS deployment 1 (green, 283m). Vertical lines represent the 95% confidence level; (e) shows spectra for the ice-free (black) and ice-covered (blue) seasons for RaTS deployment 2 (196m).



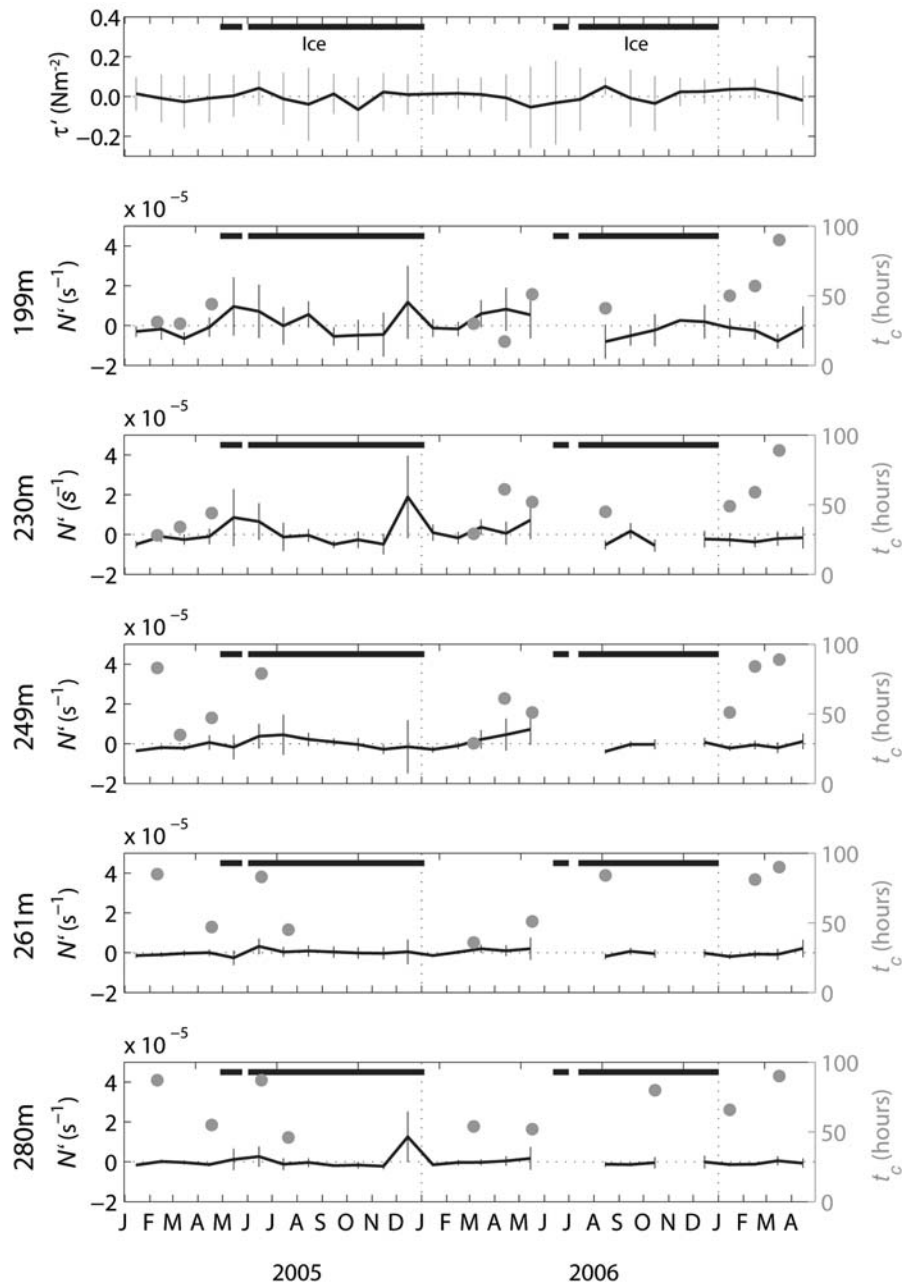
1045  
 1046  
 1047  
 1048  
 1049  
 1050  
 1051  
 1052

Figure 6: Correlations of temperature and NW-SE wind anomalies for the 30-day period 26/1/05-24/2/05 during the ice-free season of RaTS deployment 1. Both the wind and oceanographic data are filtered using a 26-hour Butterworth lowpass filter prior to correlation. The black and grey dashed lines represent the 95% and 99% significance levels, respectively.



1053  
 1054  
 1055  
 1056  
 1057  
 1058  
 1059  
 1060

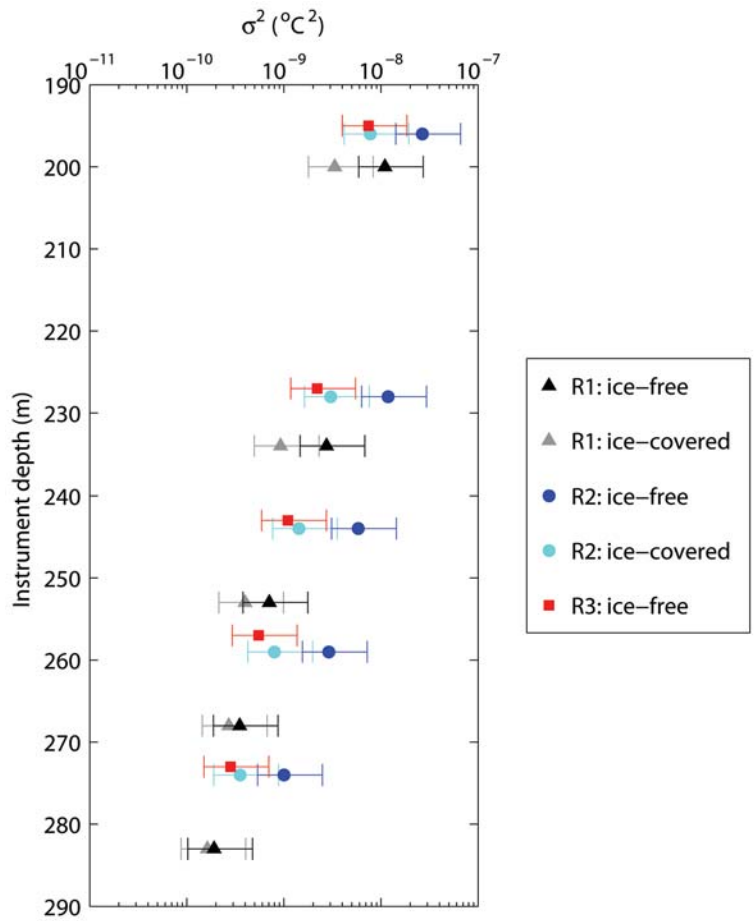
Figure 7: Log-linear plots of power spectral density (PSD) for the NW-SE wind (black) and temperature at 196m from RaTS deployment 2 during the ice-free season of 2006. Vertical lines represent the 95% confidence intervals for the wind (grey) and temperature (cyan) time series.



1061  
 1062  
 1063  
 1064  
 1065  
 1066  
 1067  
 1068  
 1069  
 1070  
 1071  
 1072

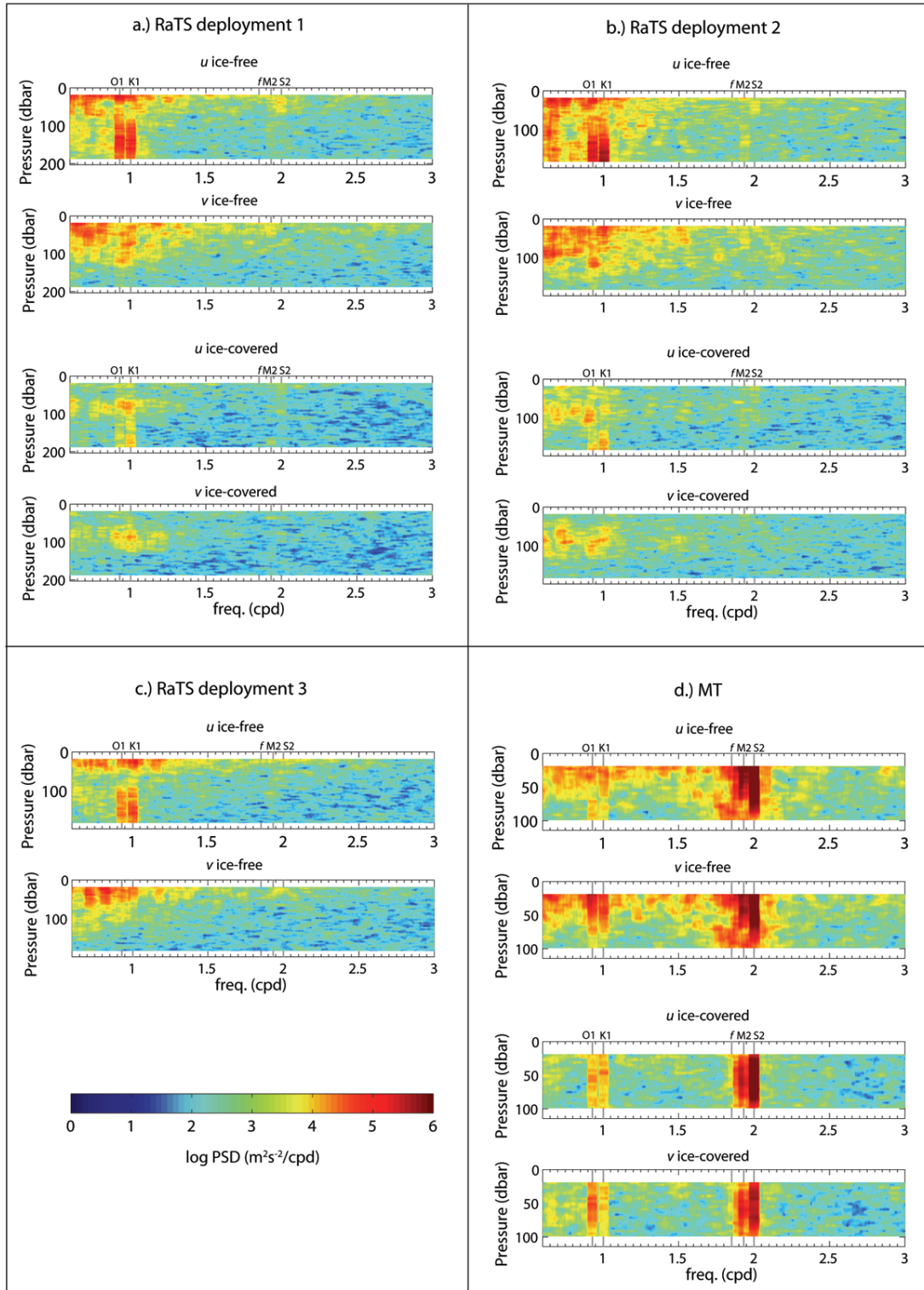
Figure 8: Time series of monthly mean NW-SE wind stress anomaly ( $\tau'$ ) at Rothera station and monthly mean buoyancy frequency anomalies ( $N'$ ) from the RaTS CTD profiles for depths corresponding to those of the five temperature sensors on the RaTS mooring (missing data are due to gaps in the CTD sampling program). Vertical lines indicate  $\pm 1$  standard deviation. The mean depth of each sensor over the three deployments is noted to the left of each plot. The timescales ( $t_c$ ) at which temperature perturbations best correlate with cumulative wind stress are marked by the grey dots (only those correlations significant at the 95% or 99% level are included). The thick black lines indicate periods of sea ice cover.





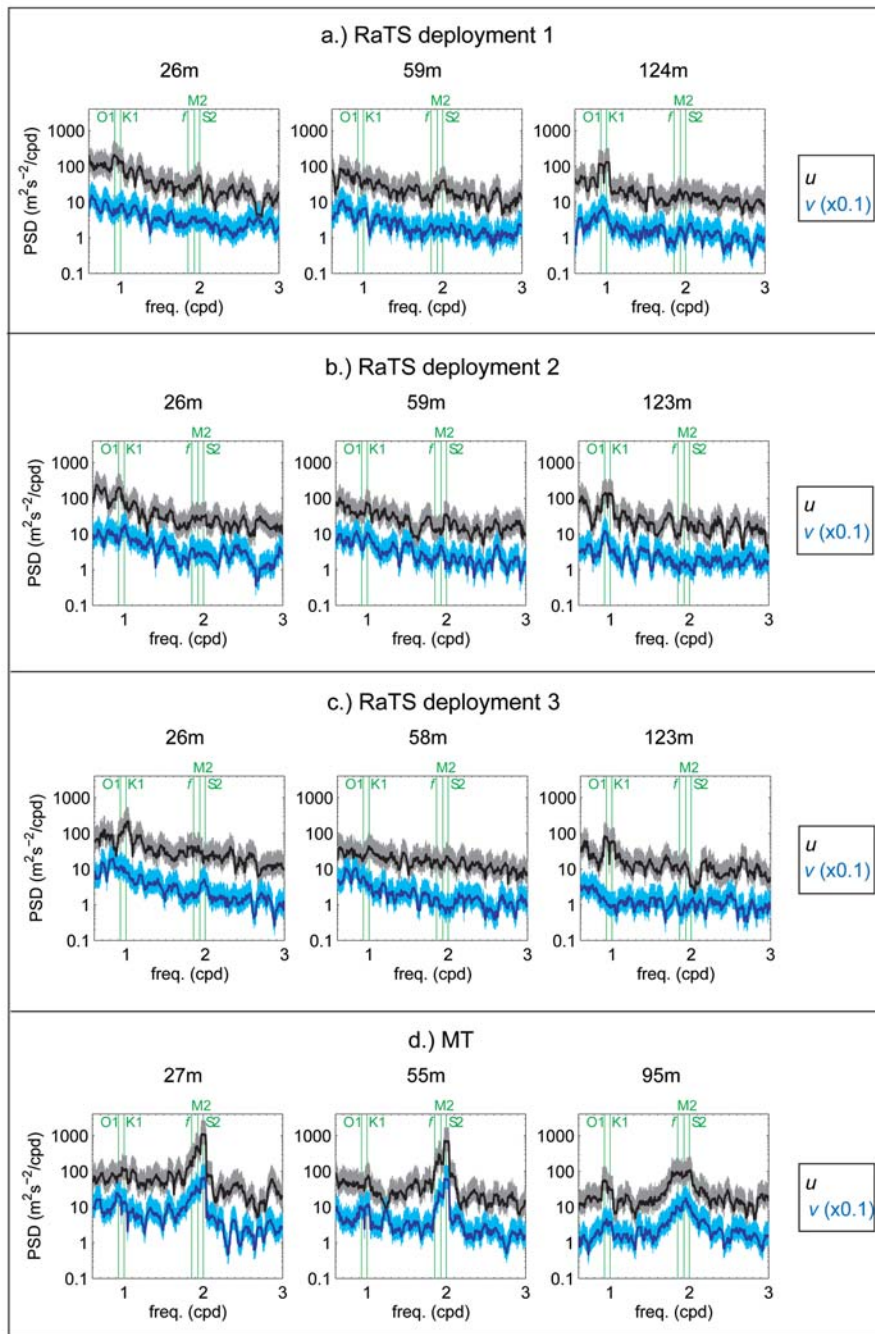
1073  
 1074  
 1075  
 1076  
 1077  
 1078  
 1079  
 1080  
 1081

Figure 9: Log-linear plot of variance ( $\sigma^2$ ) of temperature time series against instrument depth over the 2-7 day period for the ice-free and ice-covered seasons of the three RaTS deployments. Deployment 1 is represented by triangles (black and grey for the ice-free and ice-covered seasons, respectively); deployment 2 by circles (dark and light blue); and deployment 3 by red squares. Bars represent 95% confidence intervals.



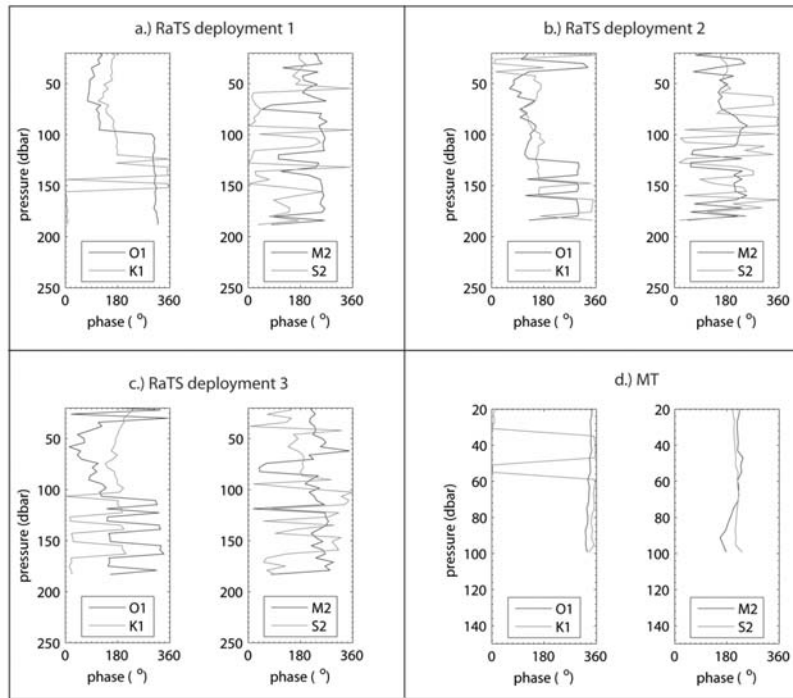
1082  
 1083  
 1084  
 1085  
 1086  
 1087  
 1088  
 1089  
 1090

Figure 10: Contour plots of power spectral density (PSD) for east ( $u$ ) and north ( $v$ ) velocities from the moored ADCPs at (a-c) the RaTS site for all deployments and (d) MT. Spectra for both the ice-free and ice-covered seasons are included, where available. The O1, K2, M2, S2 and inertial ( $f$ ) periods are marked. Note the different depth scales at the two mooring sites. Frequency measured in cycles per day.



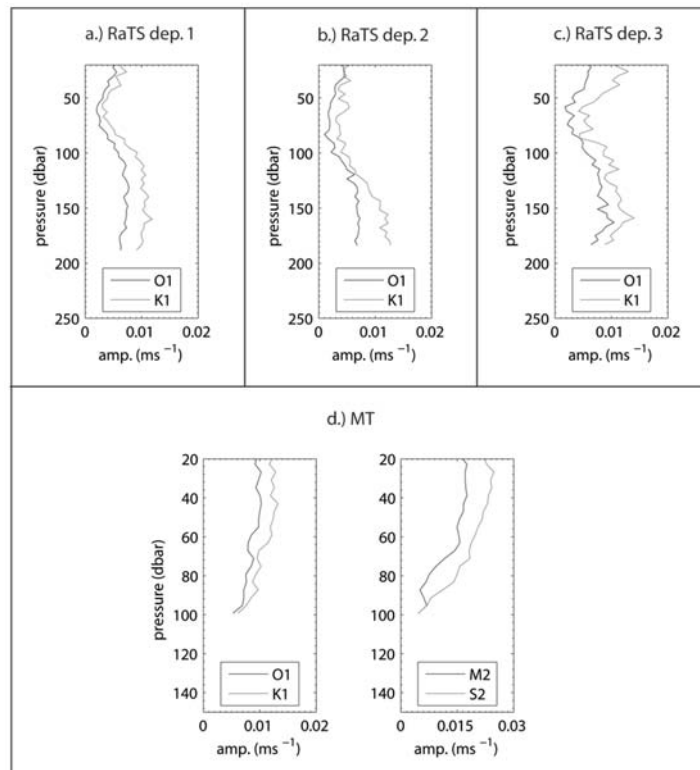
1091  
 1092  
 1093  
 1094  
 1095  
 1096  
 1097  
 1098  
 1099  
 1100

Figure 11: Confidence levels for ADCP velocity PSD for selected depths from (a-c) the three RaTS deployments and (d) MT. Eastward velocity ( $u$ ) and northward velocity ( $v$ ) are shown in black and dark blue, with their respective 95% confidence levels in grey and light blue.  $PSD(v)$  is multiplied by 0.1 for ease of viewing. Frequencies of the O1, K1, M2 and S2 semidiurnal tides are marked in light green, as is the inertial frequency,  $f$ .



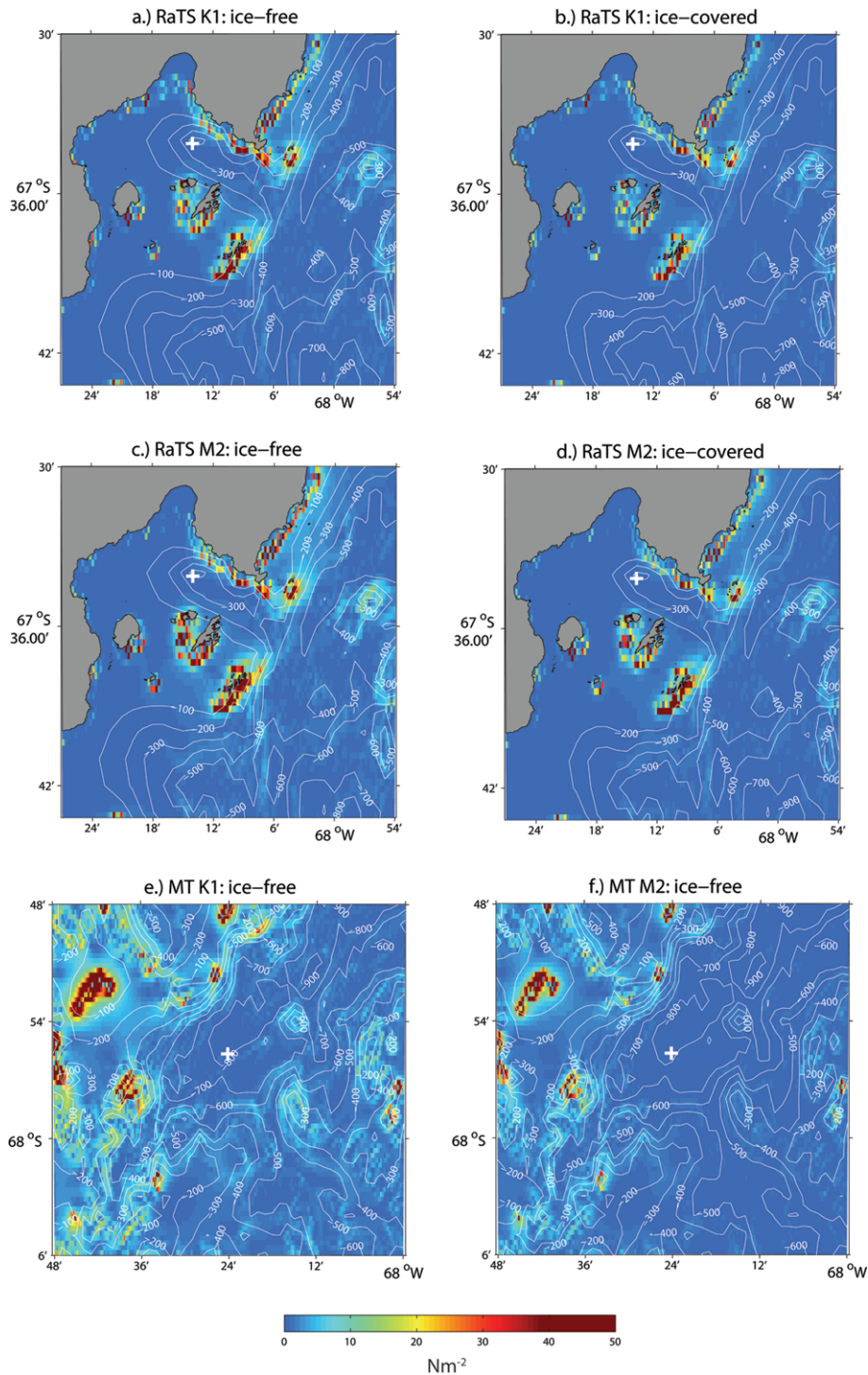
1101  
 1102  
 1103  
 1104  
 1105  
 1106

Figure 12: Profiles of tidal phase for the diurnal O1 and K1, and semidiurnal M2 and S2 tides for the three RaTS deployments and MT. Profiles are extracted from the ADCP data using the harmonic analysis package, T\_TIDE (Pawlowicz et al., 2002).



1107  
 1108  
 1109  
 1110  
 1111  
 1112

Figure 13: Profiles of tidal amplitude for the diurnal O1 and K1 tides for the (a-c) three RaTS deployments and (d) MT, and the semidiurnal M2 and S2 for MT. Profiles are extracted from the ADCP data using the harmonic analysis package, T\_TIDE (Pawlowicz et al., 2002).



1113  
 1114  
 1115  
 1116  
 1117  
 1118  
 1119  
 1120  
 1121  
 1122  
 1123  
 1124

Figure 14: Depth integrated tidal forcing function ( $F^*$ ) calculated for (a, b) the K1 and (c, d) the M2 tides during the ice-free and ice-covered seasons of RaTS deployment 1, and (e, f) the K1 and M2 tides during the ice-free season at MT. The mooring locations are signified by white crosses and contoured depths are in metres (courtesy of the SO-GLOBEC program). The land is shaded grey and detailed coastline data for Ryder Bay are courtesy of MAGIC, BAS.

Moorings	Water depth (m)	Deployment	Location (deg, min)	Deployed	Recovered	Deployment length (days)
RaTS	520	1	67° 34.02'S 68° 14.02'W	25/01/05	15/02/06	387
		2	67° 33.97'S 68° 14.06'W	17/02/06	16/12/06	303
		3	67° 34.01'S 68° 14.00'W	17/12/06	09/04/07	114
MT	840	1	67° 55.39'S 68° 24.15'W	24/01/05	15/02/06	388

1125  
1126  
1127

Table 1: Deployment details for the Marguerite Bay moorings

Instrument	Sampling period	Deployment	Depth (m) [Pressure (dbar)]
<b>RaTS site</b>			
CTD & 75kHz ADCP	CTD: 1 hour	1	200 [202]
	ADCP: 15 min.	2	196 [199]
	ensembles	3	195 [197]
TR	1 hour	1	~234
		2	~228
		3	~227
CTD	1 hour	1	253 [255]
		2	244 [246]
		3	243 [245]
TDR	1 hour	1	268 [271]
		2	259 [261]
		3	257 [260]
CTD	1 hour	1	283 [286]
		2	274 [277]
		3	273 [276]
<b>MT site</b>			
CTD & 75kHz ADCP	CTD: 1 hour ADCP: 15 min. ensembles	1	114 [115]
TR	1 hour	1	~185
TDR	1 hour	1	240 [242]
CTD	1 hour	1	298 [302]
TR	1 hour	1	~352
TDR	1 hour	1	406 [411]
CTD	1 hour	1	457 [462]
TR	1 hour	1	~511
TDR	1 hour	1	564 [571]

1128  
1129  
1130  
1131  
1132  
1133  
1134  
1135  
1136  
1137  
1138

Table 2: Mooring configurations. Abbreviations are as follows: CTD = conductivity-temperature-depth sensor; TDR = temperature-depth recorder; TR = temperature recorder; ADCP = Acoustic Doppler Current Profiler. Depths of some instruments are approximate in the absence of pressure data.

1139

Deployment	Season	Dates
1	Ice-free	26/01/05-24/02/05
		27/02/05-28/03/05
		03/04/05-02/05/05
1	Ice-covered	03/06/05-02/07/05
		06/07/05-04/08/05
		15/09/05-14/10/05
2	Ice-free	18/02/06-19/03/06
		28/03/06-26/04/06
		30/04/06-29/05/06
2	Ice-covered	30/07/06-28/08/06
		31/08/06-29/09/06
		30/09/06-29/10/06
3	Ice-free	31/12/06-29/01/07
		30/01/07-28/02/07
		02/03/07-31/03/07

1140 Table 3: Time periods over which correlations were carried out between winds at  
 1141 Rothera and moored temperature time series.

1142  
 1143

Deployment	Depth (m)	$\frac{\sigma_{no\ ice}^2}{\sigma_{ice}^2}$	$\frac{\sigma_{no\ ice}^2 [2]}{\sigma_{no\ ice}^2 [1,3]}$	$\frac{\sigma_{ice}^2 [2]}{\sigma_{ice}^2 [1,3]}$
1	200	3.29	2.41	2.33
	~234	2.97	4.31	3.29
	253	1.78	8.16	3.58
	268	1.30	8.28	2.94
	283	1.17	5.23	2.17
2	196	3.40		
	~288	3.89		
	244	4.06		
	259	3.65		
3	274	2.83		
	195		3.56	
	~227		5.38	
	243		5.26	
	257		5.27	
	273		3.56	

1144 Table 4: Comparison of variance over the 2-7 day period from the ice-free and ice-  
 1145 covered seasons for all instruments from the three RaTS deployments. Comparisons  
 1146 include variance during the ice-free season divided by variance during the ice-covered  
 1147 season; variance during the ice-free season of deployment 2 divided by the  
 1148 corresponding data from the other two deployments; and variance from the ice-  
 1149 covered season of deployment 2 divided by that from the ice-covered season of  
 1150 deployment 1.

1151  
 1152  
 1153  
 1154  
 1155  
 1156  
 1157  
 1158

Tidal con.	Freq. (cpd)	RaTS site		MT site	
		$u$ amp. (cms <sup>-1</sup> ) [phase (°)]	$v$ amp. (cms <sup>-1</sup> ) [phase (°)]	$u$ amp. (cms <sup>-1</sup> ) [phase (°)]	$v$ amp. (cms <sup>-1</sup> ) [phase (°)]
M2	1.9323	1.05 [40.32]	3.24 [186.88]	0.37 [179.53]	0.17 [321.23]
S2	2.0000	1.68 [141.95]	2.54 [254.65]	0.59 [320.86]	0.57 [193.59]
K1	1.0027	0.83 [169.57]	0.39 [294.51]	0.39 [335.22]	0.36 [211.57]
O1	0.9295	0.78 [149.15]	0.97 [273.21]	0.34 [324.49]	0.23 [205.07]

1159 Table 5: Amplitude and phase of the eastward ( $u$ ) and northward ( $v$ ) components of  
1160 the dominant diurnal and semidiurnal tides for the two mooring sites. Data are from  
1161 the AntPen04.01 tidal model (Padman, unpublished; [www.esr.org/ptm\\_index](http://www.esr.org/ptm_index)).